nature communications

Article

https://doi.org/10.1038/s41467-024-50990-x

Kinesin-14 HSET and KlpA are non-processive microtubule motors with load-dependent power strokes

Received: 31 May 2023

Accepted: 25 July 2024

Published online: 03 August 2024

Check for updates

Xinglei Liu[1,4], Lu Rao[1,4], Weihong Qiu[2], Florian Berger[3] ✉ & Arne Gennerich[1] ✉

Accurate chromosome segregation during cell division relies on coordinated actions of microtubule (MT)-based motor proteins in the mitotic spindle. Kinesin-14 motors play vital roles in spindle assembly and maintenance by crosslinking antiparallel MTs at the spindle midzone and anchoring spindle MTs' minus ends at the poles. In this study, we investigate the force generation and motility of the Kinesin-14 motors HSET and KlpA. Our findings reveal that both motors are non-processive, producing single load-dependent power strokes per MT encounter, with estimated load-free power strokes of ~30 and ~35 nm, respectively. Each homodimeric motor generates forces of ~0.5 pN, but when assembled in teams, they cooperate to generate forces of 1 pN or more. Notably, the cooperative activity among multiple motors leads to increased MT-sliding velocities. These results quantitatively elucidate the structure-function relationship of Kinesin-14 motors and underscore the significance of cooperative behavior in their cellular functions.

Accurate chromosome partitioning during cell division relies on the proper assembly and maintenance of the mitotic spindle, which is composed of polar and dynamic microtubule (MT) polymers[1]. MT-associated motors such as cytoplasmic dynein, mitotic kinesins, and non-motor MT-associated proteins (MAPs) play crucial roles in the segregation of sister chromatids toward opposite spindle poles[2,3]. Cytoplasmic dynein interacts with astral MTs at the cell membrane and separates duplicated centrosomes at the beginning of mitosis with the assistance of Kinesin-5 (Eg5 in humans and BimC in *Aspergillus nidulans*), which pushes the interacting interpolar MTs of opposite polarity apart. To counterbalance the outward directed forces generated by Kinesin-5 and prevent excessive separation of the two opposing MT arrays while the spindle forms, Kinesin-14 motors (HEST in humans and KlpA in *A. nidulans*) generate the opposing inward directed forces[2,4,5].

Unlike members of the Kinesin-5 family of motor proteins, which form tetramers with two motor domains at each end of a central stalk[6,7], Kinesin-14 members function as dimers, equipped with C-terminal motor domains and N-terminal MT-binding tail domains, to crosslink and slide MTs[8–10]. These motors have diverse roles in the assembly and regulation of the mitotic spindle. For example, *Schizosaccharomyces pombe* Kinesin-14 Pkl1 localizes to spindle poles to anchor the minus ends of spindle MTs, while *S. pombe* Kinesin-14 Klp2 crosslinks antiparallel MTs from opposite poles within the midzone to counteract the outward pushing forces generated by Kinesin-5 Cut7[8]. HSET and *Xenopus laevis* Kinesin-14 XCTK2 affect spindle length and morphology through MT sliding[11]. Not surprisingly, dysfunction or dysregulation of Kinesin-14 motors can lead to impaired cell division, including defective spindle assembly and erroneous chromosome segregation[12–16].

Structure-function studies have provided valuable insights into the molecular functions of Kinesin-14 motors[17–26]. However, despite extensive efforts to understand their mechanisms, a consensus regarding the precise molecular function of Kinesin-14 motors remains elusive. For instance, studies have shown that single Ncd molecules (a

[1]Department of Biochemistry and Gruss Lipper Biophotonics Center, Albert Einstein College of Medicine, Bronx, NY, USA. [2]Cell Biology, Neurobiology and Biophysics, Department of Biology, Faculty of Science, Utrecht University, CH Utrecht, The Netherlands. [3]Department of Biochemistry & Biophysics and Department of Physics, Oregon State University, Corvallis, OR, USA. [4]These authors contributed equally: Xinglei Liu, Lu Rao. ✉e-mail: f.m.berger@uu.nl; arne.gennerich@einsteinmed.edu

Kinesin-14 motor in *Drosophila melanogaster*) are non-processive, minus-end-directed motors, performing a single ATP-triggered power stroke per MT encounter[18,22,27–30]. On the other hand, KlpA exhibits processive movement towards the MT plus end at the single-molecule level but displays canonical minus-end-directed motility in multi-motor-based MT-gliding and -sliding assays[17]. Furthermore, while single Ncd molecules generate forces of ~0.5 pN[19,23,24], single HSET molecules have been suggested to generate forces of up to 1.1 pN by taking multiple processive steps along MTs[25]. Consequently, it remains uncertain whether these reported differences are species-specific or arise from variations in experimental conditions such as the choice of assay, buffer conditions, and protein preparations.

Here, by combining structure-function studies with single-molecule fluorescence and optical tweezers assays, we demonstrate that HSET and KlpA behave as non-processive motors under load (when attached to a cargo), producing single power strokes per MT encounter. Our findings suggest that, under load-free conditions, full-length HSET and KlpA generate effective power strokes of ~30 and ~35 nm, respectively. However, as the applied load increases, their power stroke are hindered, resulting in reduced displacements of ~2 and ~3 nm, respectively, under an applied load of ~0.7 pN. This load-dependency of the lever arm, combined with its limited length, provides an explanation for why Kinesin-14 motors generate forces below 1 pN at the single-molecule level.

Contrary to previous studies that reported a decrease in MT-gliding velocity with an increased number of motors[20,31], our findings reveal that multiple HSET/KlpA/Ncd molecules work synergistically to achieve higher velocities in MT-gliding assays. When assembled into oligomers or other multi-motor configurations, these motors not only exhibit processive motion toward the MT minus end under both unloaded (our data and refs. 17,19,21,32) and loaded conditions but also are capable of generating forces exceeding 1 pN. This demonstrates that, while individually, Kinesin-14 motors act as non-processive and low-force-generating motors when connected to cargoes such as antiparallel MTs or, as in our experimental setup, optical trapping beads, they exhibit enhanced processivity and force generation in collective configurations.

Results

KlpA is non-processive under load

The force-generation capability of the *D. melanogaster* Kinesin-14 Ncd has been extensively studied at the single-molecule level[19,23,24,33,34]. In contrast, the force generation of the *A. nidulans* Kinesin-14 KlpA remains unexplored. Unlike Ncd, which is non-processive and generates a single ATP-triggered working stroke towards the MT minus end with each MT encounter[18,22,27–30], KlpA is a processive motor that moves towards the MT plus end[17]. The processivity of KlpA critically depends on its N-terminal MT-binding tail, as KlpA lacking the N-terminal tail behaves like a non-processive motor[17].

To investigate KlpA's behavior under load, we engineered a GFP-tagged full-length KlpA construct for the coupling of the N-terminal tail to anti-GFP antibody-coated polystyrene trapping beads (Fig. 1A, B and Suppl. Fig. 1A). To assess the force-generation capability of single KlpA molecules, we conducted optical-trapping experiments at motor concentrations where less than 30% of the beads interacted with the coverslip-attached MTs[35] (Fig. 1B, C). When the tail of KlpA was bound to a 1-µm trapping bead, it generated a force of ~0.5 pN towards the MT minus-end (Fig. 1C, D and Suppl. Fig. 2), slightly higher than the force produced by Ncd, where two Ncd molecules linked through a DNA scaffold generate approximately 0.5 pN[19]. Notably, the MT-binding tail domain of KlpA, which facilitates processive motility in the absence of its attachment to an anti-parallel MT[17], ceases to assist KlpA's processive motion once bound to a polystyrene trapping bead. This non-processive state persists even after deactivating the optical trap; following deactivation, beads diffuse away from the MT at the single-molecule level (Suppl. Fig. 3A), while under multi-motor conditions, beads exhibit processive motility along MTs (Suppl. Fig. 3B). These observations suggest that the mere attachment of the cargo bead to the MT-binding tail domain is sufficient to alter KlpA's motility, confining it to single power strokes (Fig. 1C, right). In the absence of ATP, KlpA binds to MTs without causing a detectable displacement, confirming that the detected power strokes are driven solely by ATP binding/hydrolysis[18,23] (Suppl. Fig. 4). Furthermore, in contrast to previous force measurements on Ncd that reported a displacement component also in perpendicular direction[23,24], KlpA generates power strokes exclusively along the long MT axis (Fig. 1E).

Multiple KlpA molecules work cooperatively to generate larger forces

KlpA has been shown to form oligomeric complexes comprising multiple motors that move processively towards the MT minus end[17]. To investigate KlpA's cooperative behavior under load, we conducted force measurements with varying KlpA concentrations while keeping the bead concentration constant. To distinguish between KlpA's self-oligomerization, which occurs with increasing motor concentrations (Fig. 1F), and the recruitment of individual KlpA molecules to the bead surface via anti-GFP antibodies, we introduced increasing concentrations of mCherry-tagged KlpA motors (Suppl. Fig. 1B) to beads that were pre-bound to GFP-tagged KlpA motors. The concentration of GFP-tagged motors was carefully selected to ensure that <30% of the pre-coated beads exhibited force-generation events, suggesting the presence of only one GFP-tagged motor per force-generating bead[35]. Unlike Kinesin-1, which shows minimal dependence on the number of motors[19,36,37], multiple KlpA motors cooperatively generate forces of 1 pN and higher (Fig. 1G). This cooperative behavior in KlpA resembles that of Ncd, which also generates additive forces when multiple motors are engaged[19]. Although non-specific motor-bead interactions were observed at higher concentrations of added mCherry-KlpA, the increase in force generation upon adding mCherry-KlpA was also influenced by KlpA oligomerization (Fig. 1G, H and Suppl. Fig. 5A). This statement is supported by our observation that the force generation consistently increases in the presence of mCherry-KlpA when the trapping beads are pre-bound to a single GFP-tagged motor, facilitating oligomerization with mCherry-tagged motors (Suppl. Fig. 5A).

HSET is a non-processive motor that cooperates when working in teams

Contrasting with previous studies on Ncd[19,23,24,34] and our findings on KlpA (Fig. 1C, D), recent research suggests that HSET, the human Kinesin-14 ortholog, is processive, capable of multiple 8-nm steps under loads up to ~1.1 pN[25]. To explore differences under load between KlpA and HSET, we examined full-length, GFP-tagged HSET (Fig. 2A and Suppl. Fig. 1C) using optical-trapping experiments. Surprisingly, HSET generated an average force of 0.5 pN (Fig. 2C, D and Suppl. Fig. 6), contrary to earlier reports[25] but aligned with our KlpA results (Fig. 1C, D). Further mirroring our findings with KlpA (Fig. 1E), HSET also produced displacements solely along the long MT axis (Suppl. Fig. 7A). Photobleaching experiments on MT-bound HSET in a strong binding state (induced by AMP-PNP[18]) predominantly showed two bleaching steps (Fig. 2G and Suppl. Fig. 8), indicating HSET mainly forms homodimers, with a smaller proportion (~16%) forming tetramers, corroborated by native-gel analysis (Suppl. Fig. 9). This finding agrees with our observations on KlpA (Fig. 1H) and is further supported by fluorescence microscopy, which revealed that at higher concentrations, HSET not only forms higher-order particles but also exhibits processive movement towards the MT minus end (Fig. 2H and Suppl. Fig. 10A).

Force measurements across varying HSET concentrations fit a model for a single or more motors, rather than a model for two or more motors[35] (Fig. 2B), confirming the ~0.5 pN force is generated by a single

https://doi.org/10.1038/s41467-024-50990-x

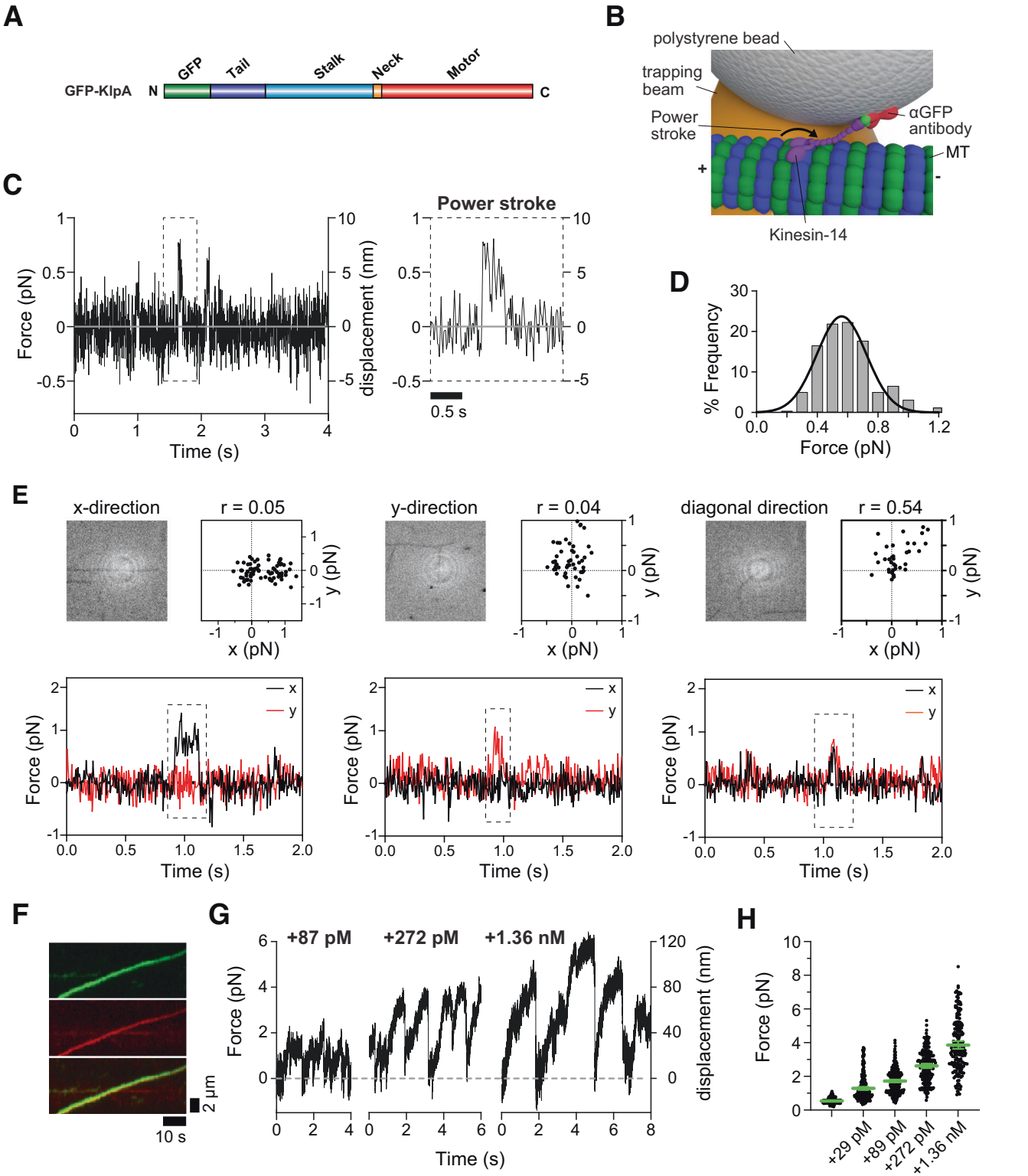

HSET dimer. Our analysis showed non-processive "power strokes" (Fig. 2C, right), similar to KlpA (Fig. 1C, right) and Ncd[23,24]. However, at higher HSET concentrations, forces exceeded 1 pN (Fig. 2I, J), supporting our hypothesis that HSET's reported 1.1 pN force[25] is due to the cooperative activity of multiple molecules. Our findings further revealed that multiple HSET molecules advance the trapping beads in ~8 nm increments (analyzed for forces up to 1.5 pN) with dwell times in between steps fitting a single exponential function (Suppl. Fig. 11). These multi-motor transport properties are significant because the previous study suggested such movement pattern indicated single-motor activity[25]. In contrast, our results demonstrate that these 8-nm steps and exponential dwell times can also occur with multiple motors working in a team. These findings challenge earlier interpretations and underscore the complexity of HSET's multi-motor force generation. In summary, individual HSET molecules demonstrate non-processive, weak force generation, but in groups, they cooperate to generate significantly larger forces, paralleling the behavior seen in KlpA (Fig. 1G, H) and Ncd[19].

Fig. 1 | KlpA force generation in isolation and in teams. A Structural organization of the full-length recombinant GFP-KlpA construct: tail (a.a. 1-152), central stalk (a.a. 153-416), neck (a.a. 417-421), and catalytic motor domain (a.a. 422-756). **B** Optical-trapping assay: polystyrene bead with a bound Kinesin-14 motor trapped by a near-infrared beam, positioned above a surface-bound MT (not to scale). **C** Left: Force-versus-time trace of bead movement driven by a single KlpA molecule at 1 mM ATP and k_{trap} = 0.1 pN/nm. Right: Highlighted trace section showing a single-step displacement ("power stroke") corresponding to the rectangular box on the left. **D** Histogram of forces generated by single KlpA molecules (0.56 ± 0.01 pN, mean ± SEM from Gaussian fit, n = 260, k_{trap} = 0.1 pN/nm; source data are provided as a Source Data file). **E** Full-length KlpA exhibits power strokes towards the MT minus end, with no detectable displacements in the normal direction (Pearson correlation coefficient, $-0.2 < r < 0.2$). Top row: IRM images of horizontally and vertically oriented MTs and x-y position plots with Pearson correlation values. Bottom row: x (black) and y (red) direction signals. Diagonal MT orientation shows displacements in both directions (right) (k_{trap} = 0.1 pN/nm) (source data are provided as a Source Data file). **F** Example of MT minus-end-directed processive motion of a KlpA oligomer consisting of GFP- and mCherry-tagged KlpA molecules formed by adding 150 pM GFP-KlpA and 150 pM mCherry-KlpA to the slide chamber (source files are provided as a Source Data file). **G** Force traces of GFP-KlpA bound to anti-GFP antibody-coated beads, oligomerized with increasing mCherry-KlpA: +87 pM (left), +272 pM (middle) and +1.36 nM (right). **H** Forces generated by oligomerized KlpA motors at different mCherry-KlpA concentrations (k_{trap} = 0.05 pN/nm) (source data are provided as a Source Data file). Green bars represent the mean with 95% confidence intervals (CIs). GFP-KlpA at the single-molecule level (14 pM) without added mCherry-KlpA: 0.51 ± 0.01 pN (mean ± SEM, n = 493); +29 pM mCherry-KlpA: 1.29 ± 0.05 pN (n = 232); +87 pM mCherry-KlpA: 1.73 ± 0.04 pN (n = 259); +272 pM mCherry-KlpA: 2.62 ± 0.07 pN (n = 203); and +1.36 nM mCherry-KlpA: 3.86 ± 0.12 pN (n = 187). Note: a.a. refers to amino acid.

Full-length and tail-truncated HSET behave indistinguishably under load

A previous study also indicated that the N-terminal MT-binding tail of HSET may affect the motility of HSET-coated beads under unloaded conditions[25]. However, in the optical-trapping assay, where the tail is pulled away from the MT surface due to its coupling to the trapping bead, its interaction with MTs is unlikely. Based on this understanding, we hypothesized that the force generation of HSET without the N-terminal tail would be similar to full-length HSET. To test this hypothesis, we expressed a tail-truncated HSET construct with an N-terminal GFP (GFP-HSETΔTail, Fig. 2A) and examined its force generation. Like full-length HSET, single tail-truncated HSET molecules generated forces of ~0.5 pN (Fig. 2E, F and Suppl. Fig. 12). Additionally, at the multi-motor level, GFP-HSETΔTail exhibited cooperative behavior to generate larger forces (Suppl. Fig. 10B). These findings demonstrate that both KlpA and HSET exhibit comparable force generation capabilities at both the single- and multi-motor level.

HSET and KlpA perform a single power stroke to generate 0.5 pN

The force generated by single Kinesin-14 molecules, such as HSET and KlpA, is significantly weaker (~0.5 pN; Figs. 1C, D and 2C, D) than that generated by Kinesin-1 (~5 pN[38,39]) and Kinesin-3 (~3 pN[38,40]). To investigate why HSET and KlpA produce only ~0.5 pN, we examined the cryoEM structure of Ncd[18], which suggested that despite having two motor domains, Ncd generates only a single ~9 nm power stroke per interaction with the MT (MT binding, power stroke, followed by detachment) (Fig. 3A). Based on these results, we hypothesized that if the power-stroke size remains constant regardless of the applied load, the force output in the trapping assay should increase with higher trap stiffness (corresponding to a higher force per unit displacement). To test this hypothesis, we measured the force generation of single KlpA and HSET molecules as a function of trap stiffness and discovered that the force output indeed increased with increasing trap stiffness up to 0.3 pN/nm (Fig. 3B and Suppl. Fig. 13A). However, this increase in force was accompanied by a reduction in power-stoke size, suggesting that the lever-arm movement of Kinesin-14 is increasingly constrained under higher loads. At the lowest trap stiffness examined (0.05 pN/nm), KlpA and HSET generated displacements of ~10 and ~8 nm (Fig. 3C and Suppl. Fig. 13B), respectively, aligning with the cryoEM findings.

However, the Ncd cryoEM study also reported on MT-gliding assays and measured ATPase activities to estimate the power-stroke size for different tail-truncated Ncd constructs[18]. For the longest Ncd construct studied (encoding amino acids 236-700), the estimated lever-arm length was ~16 nm, which is more than the power-stroke length suggested by the structural analysis[18]. Given that Ncd is non-processive, the velocities obtained from a MT-gliding assay depend not only on the power-stroke sizes but also on the density of Ncd motors fixed to the cover glass. This complexity suggests that a comparison of ATPase activities with MT-gliding velocities might not yield reliable estimates for the power-stroke length for Ncd.

To estimate the load-free power-strokes for full-length KlpA and HSET, we first accounted for the combined compliance of the motors and the GFP-antibody linkage by modeling the motors' stiffness using a worm-like chain (WLC) model, a non-linear force-extension equation often used to model the force-induced stretching of DNA[41] and proteins[42–44], as detailed in the Methods section (see also Fig. 3D, E and Suppl. Fig. 13C, D). Our findings show that while the measured power strokes of KlpA decrease with increasing trap stiffness (Fig. 3C), the estimated load-free power-stroke length remains independent of the trap stiffness, as expected (Fig. 3E), since the motors' stiffness should not dependent on the optical trap power settings. After adjusting for the size of the GFP-antibody complex, we obtained load-free power strokes of 35 ± 3 nm and 31 ± 2 nm (mean ± propagated error; see "Methods" section for a detailed description of the error calculation) for KlpA and HSET, respectively (Fig. 3E and Suppl. Fig. 13D). While there is some uncertainty about the size of the GFP-antibody complex and how it adheres to the bead surface, we estimate the length of the complex to be 8 nm (Suppl. Fig. 25).

The longest Ncd construct previously studied consisted of only 112 amino acids in the tail[18], whereas the tails of full-length HSET and KlpA extend to 310 and 421 amino acids, respectively (Suppl. Figs. 14 and 15). This led us to hypothesize that the additional coiled-coil segments in the tails of KlpA and HSET contribute to their longer lever arms. Supporting this hypothesis, experiments with a tail-truncated KlpA construct (123 amino acids, encoding amino acids 298–770) yielded an estimated load-free power-stroke of 28 ± 2 nm, after accounting for the GFP-antibody linkage (Suppl. Figs. 16 and 17). Additionally, an Ncd construct with a tail comprising 139 amino acids (encoding amino acids 209–700, instead of the original 236-700[18]) resulted in an estimated load-free power-stroke of 29 ± 2 nm exclusively along the long MT axis (Suppl. Figs. 7B, 18, and 19). Therefore, our findings suggest that the lever-arm length of Kinesin-14 motors is considerably larger than previously suggested and occurs solely along the long MT axis.

Given potential experimental limitations, notably a rotation of the trapping bead and a decrease in the bead's height above the MT surface as a result of the power stroke (Suppl. Fig. 20), we acknowledge that our measurements might underestimate the actual power-stroke size. Therefore, they should be considered as lower bounds of the actual values. However, AlphaFold[45] predicts extensive alpha-helical coiled-coils in the tail domains of KlpA, HSET, and Ncd, estimating lengths of approximately 32, 25, and 22 nm, respectively (Suppl. Figs. 14 and 15). This suggests that our estimates are close to the predicated coiled-coil values, and our tail-truncation experiments confirm that even the distant parts of these coiled-coils indeed contribute to the power stroke.

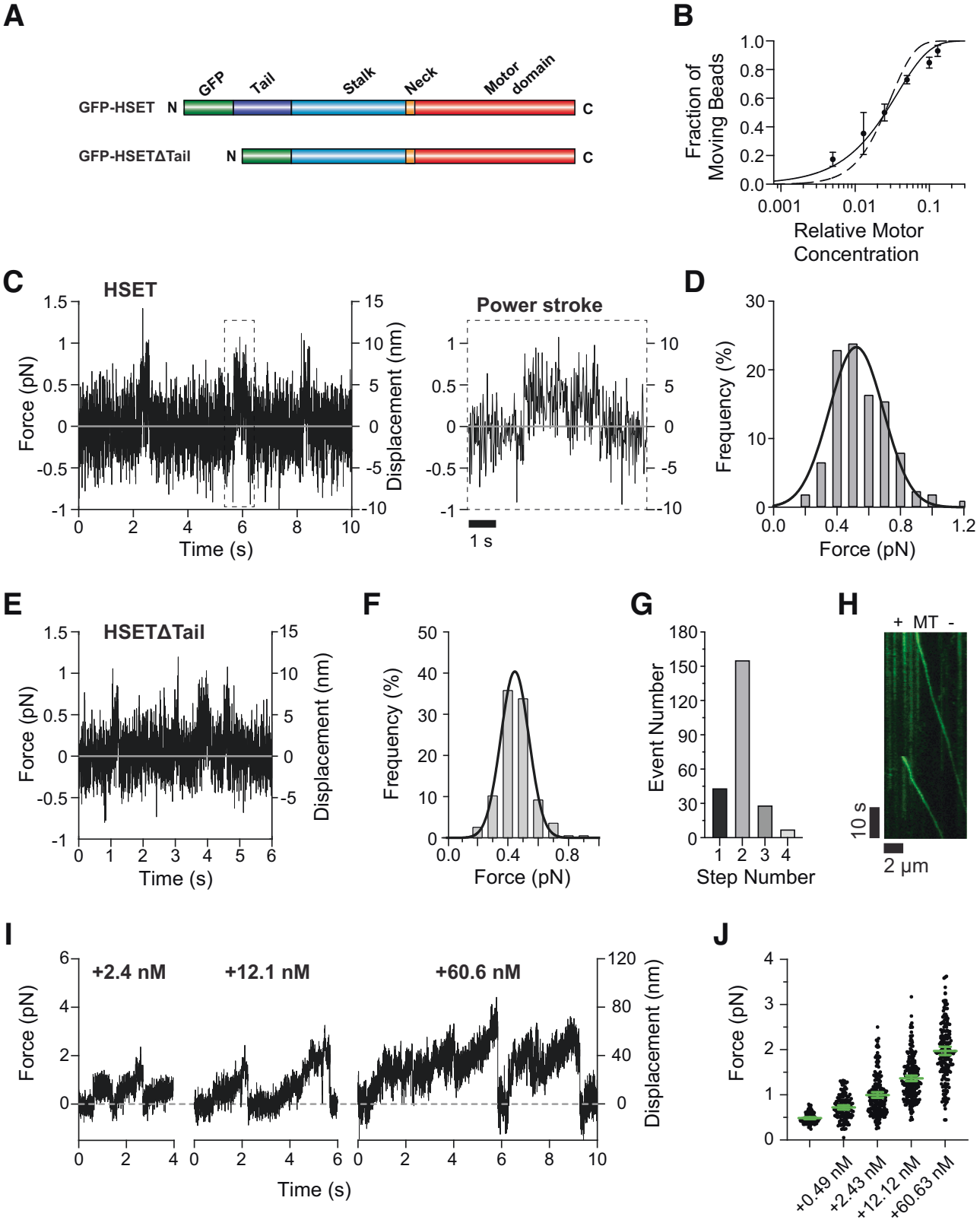

In conclusion, our findings reveal that Kinesin-14 motors exhibit power-stroke sizes significantly larger than previously reported. We also observed a trend of decreasing power-stroke size with increasing load (Fig. 3C), indicating that the lever-arm movement becomes increasingly restricted under hindering loads. This trend is particularly noticeable in the reduced displacements per MT encounter at high trap stiffnesses (Fig. 3C and Suppl. Figs. 13B, 16B and 18B), suggesting that the full potential of the power stroke is realized under conditions of low or no load. These insights highlight the importance of cooperative activities among multiple motors under physiological conditions, where Kinesin-14 work together to achieve significant displacements despite high loads.

Fig. 2 | HSET and HSETΔTail behavior under load. A Structural organization of full-length HSET (GFP-HSET) and tail-truncated HSET (GFP-HSETΔTail): tail (a.a. 1-138), central stalk (a.a. 139-305), neck (a.a. 306-310), and catalytic motor domain (a.a. 311-673). **B** Fraction of GFP-HSET-coated beads binding to and moving along MTs vs. relative motor concentration. The bead concentration was constant, while the motor concentration was varied ($n = 321$ total number of beads tested; number of beads tested at each relative concentration: 0.005: $n = 76$; 0.013: $n = 43$; 0.025: $n = 47$; 0.05: $n = 48$; 0.1: $n = 46$; and 0.13: $n = 61$). The data are represented as mean values ± standard deviation (two technical replicates were performed). Solid line: fit to the Poisson distribution 1 - exp(-λC) for one or more motor molecules, where C is the relative motor concentration and λ is a fit parameter ($R^2 = 0.933$); dotted line: fit to the distribution 1−exp(−λC)−(λC) exp(−λC) for two or more molecules ($R^2 = 0.802$) (source data are provided as a Source Data file). **C** Force-versus-time trace of bead movement driven by a single HSET molecule at 1 mM ATP and $k_{trap} = 0.1$ pN/nm. **D** Histogram of forces by single HSET molecules (0.52 ± 0.02 pN, mean ± SEM from Gaussian fit, $n = 214$, $k_{trap} = 0.1$ pN/nm) (source data are provided as a Source Data file). **E** Force-versus-time trace of bead movement by a single HSETΔTail molecule at 1 mM ATP and $k_{trap} = 0.1$ pN/nm. **F** Histogram of forces by single HSETΔTail molecules (0.45 ± 0.01 pN, mean ± SEM from Gaussian fit, $n = 197$, $k_{trap} = 0.1$ pN/nm) (source data are provided as a Source Data file). **G** Photobleaching analysis of GFP-HSET: one (44), two (156), three (29) and four (8) photobleaching steps (source data are provided as a Source Data file). **H** Example of MT minus-end-directed processive motion of HSET oligomers formed at 1 nM motor concentration. **I** Force traces of assemblies of GFP-HSET molecules at increasing concentrations of added GFP-HSET motors: +2.4 nM, +12.1 nM, and +60.6 nM. **J** Forces by GFP-HSET motors at varying concentrations of added motors ($k_{trap} = 0.1$ pN/nm). Mean values with 95% Cis: single GFP-HEST: 0.48 ± 0.01 pN (mean ± SEM, $n = 116$); +0.49 nM: 0.72 ± 0.02 pN ($n = 128$); +2.43 nM: 1.0 ± 0.03 pN ($n = 201$); +12.12 nM: 1.36 ± 0.03 pN ($n = 232$); and +60.63 nM: 1.97 ± 0.05 pN ($n = 191$) (source data are provided as a Source Data file).

Kinesin-14 motors work cooperatively to increase the velocity during MT gliding

Kinesin-14 motors, which play a critical role in sliding anti-parallel MTs within the mitotic spindle[2], differ from the processive Kinesin-1 motors[19,36]. Unlike Kinesin-1, Kinesin-14 motors engage in non-processive interactions with MTs and demonstrate cooperative force generation, similar to the non-processive muscle myosin-2 that drives muscle contraction[46–48]. As myosin-2[48,49], non-processive Kinesin-14 motors, such as HSET, KlpA, and Ncd, briefly engage with an MT to perform a power stroke before detaching (Fig. 2C, right). Given their low duty ratio (the fraction of time the motor spends bound to the filament is less than 0.5), it might be expected that the velocity of anti-parallel MTs slid inward by HSET would increase with the number of stochastically binding motors. However, studies on HSET, Ncd, and the *Xenopus laevis* Kinesin-14 XCTK2 have shown that the velocity in MT-gliding assays (Fig. 4A) decreases as the number of motors increases[20,31,50]. We replicated this unexpected result using full-length HSET and full-length Ncd (Fig. 4C and Suppl. Fig. 21A). Although we immobilized the GFP-tagged motors on the cover-glass surface using anti-GFP antibodies and employed casein to prevent non-specific binding, we hypothesized that some motors might non-specifically bind to the surface such that their N-terminal tails could act as brakes by binding to the gliding MTs to slow down gliding (Fig. 4A). To test this hypothesis, we performed a control experiment without surface-bound anti-GFP antibodies, allowing full-length HSET to non-specifically absorb onto the coverslip of the microfluidic slide chamber (Fig. 4B). As anticipated, we observed MT gliding and a reduction in gliding speed with increasing motor concentrations even in the absence of surface-absorbed antibodies (Fig. 4D), confirming that non-specifically interacting motors contribute to the decrease in gliding velocity.

Further experiments with tail-truncated HSET and tail-truncated Ncd (GFP-HSETΔTail, Fig. 2A, and GFP-NcdΔTail) revealed an increase in MT-gliding velocity with higher motor concentrations (Fig. 4E and Suppl. Fig. 21B), as expected for a motor with a low duty ratio. Additionally, increasing the ionic strength lessened the effect of motor concentrations on MT-gliding velocity driven by full-length HEST at 200 mM KCl (Fig. 4F), and resulted in an overall increase in gliding velocity with increased salt concentrations (Fig. 4G), whereas the velocity of the tail-truncated HSET did not increase with increasing ionic strength (Fig. 4H). This supports the idea that HSET's tail engages in strong ionic interactions with MTs, whereas the interactions between the motor domain and MTs are less affected by ionic strength changes. At higher ionic strengths, the motor domain's weaker MT affinity may lead to increased velocity, although this could be offset by shorter binding times during the power stroke, thus reducing velocity.

Consequently, multiple Kinesin-14 molecules collaborate, with their tails binding to adjacent MTs (not the same MT), enhancing both force generation and velocity during MT sliding. Further supporting the role of the tail in determining power-stroke length, while the velocity of KlpA-powered MT-gliding increased when the MT-binding tail sequence was removed (a construct encoding amino acids 250-770 instead of 1-770), the velocity decreased when the tail was further truncated from 520 to 472 amino acids (encoding amino acids 298-700 instead of 250-700) (Suppl. Fig. 21C), suggesting that these distant tail sequences contribute to the motors lever arm. In support of this conclusion, AlphaFold predicts alpha-helical coiled-coils up to amino acid 196 (Suppl. Figs. 14A and 15).

Discussion

This study presents a comprehensive analysis of the force generation and motility of Kinesin-14 motors, specifically addressing previous inconsistencies through structure-function studies and single-molecule analyses. Our results clarify that both KlpA from *A. nidulans* and its human counterpart, HSET, exhibit non-processive behavior under load. Despite having two motor domains, they perform a single power stroke per MT encounter, generating relatively weak forces of about 0.5 pN. However, when Kinesin-14 motors function collectively as a team, they display remarkable processivity and can generate forces of 1 pN and higher.

The finding that KlpA generates a ~ 0.5 pN force towards the MT minus end and behaves non-processively under load (Fig. 1C, D) might be unexpected as we previously demonstrated that KlpA moves processively towards the MT plus end in the absence of load[17]. Typically, processive kinesin motors generate forces of 1 pN or more[38,51–53]. However, we have shown that KlpA's processivity depends on its N-terminal MT-binding tail, as removal of this tail abolishes its ability to move processively[17]. In our trapping assay, KlpA's tail is bound to a polystyrene bead, mimicking its in vivo role of cross-linking two anti-parallel MTs. This configuration prevents the tail from interacting with the same MT as the motor domains (if the tail would bind to the same MT as the motor domains, the motor would not contribute to MT sliding), thereby explaining the non-processive behavior of KlpA under load.

In contrast to KlpA, both HSET and Ncd are non-processive in single-molecule fluorescence assays[19–21]. However, when a flexible polypeptide is inserted into the central stalk domain of KlpA and Ncd, both motors exhibit processive movement towards the MT minus end[17]. This observation underscores the importance of both the MT-binding tails and the stiffness or flexibility of the dimerizing stalk in determining the motors' processive capabilities[17]. Once the tail is bound to its cargo, such as a neighboring, antiparallel MT in the mitotic spindle or a polystyrene trapping bead, the flexibility of

https://doi.org/10.1038/s41467-024-50990-x

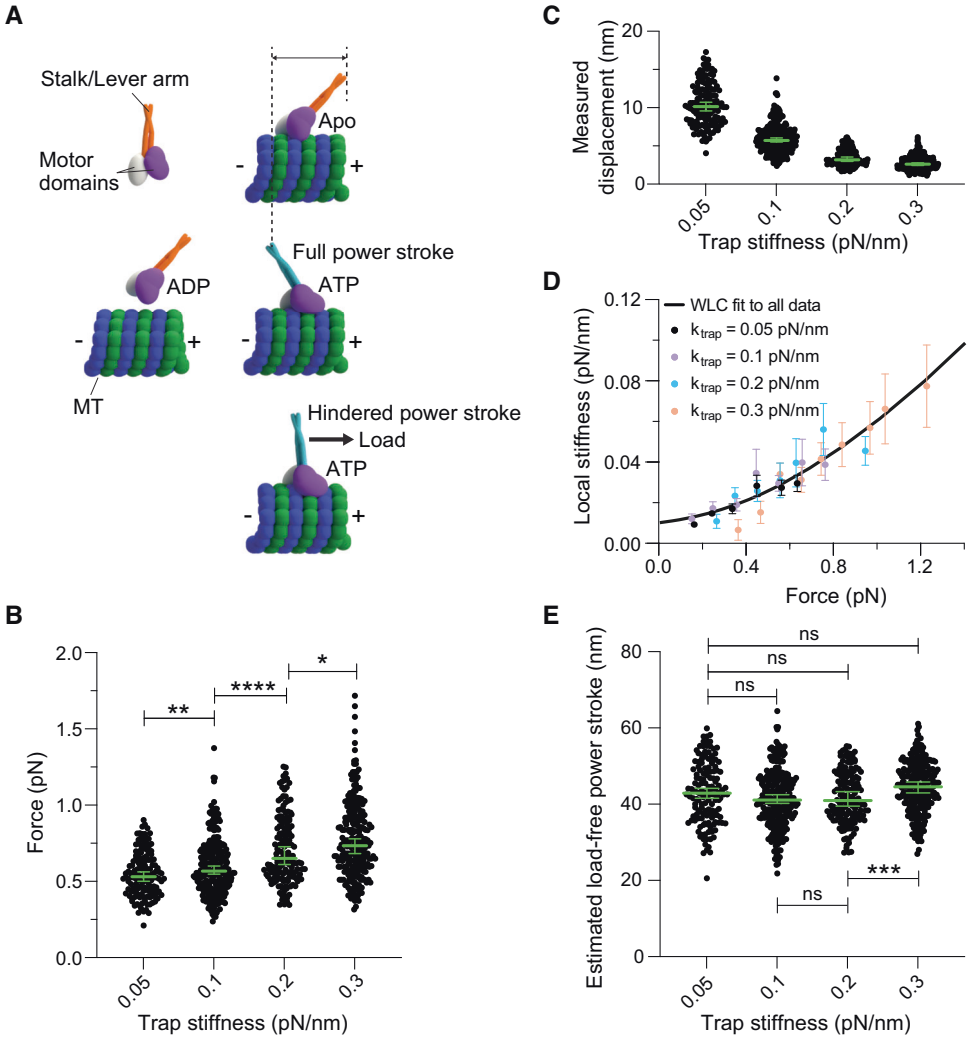

Fig. 3 | KlpA power stroke and force generation as a function of trap stiffness. **A** Schematic representation of the power stroke by KlpA/HSET under no load or low load conditions, and restrained power stroke under increased loads. **B** Force generated by single full-length KlpA molecules as a function of increasing trap stiffnesses. Green bars indicate the median values with 95% CIs. k_{trap} = 0.05 pN/nm: 0.53 (0.50, 0.56) pN (n = 142); k_{trap} = 0.1 pN/nm: 0.57 (0.55, 0.60) pN (n = 260); k_{trap} = 0.2 pN/nm: 0.65 (0.61, 0.72) pN (n = 156); and k_{trap} = 0.3 pN/nm: 0.73 (0.68, 0.78) pN (n = 247). Statistical significance was determined using a two-tailed unpaired Welch's t-test (*P = 0.0126; **P = 0.0075; ****P < 0.0001) (source data are provided as a Source Data file). **C** As in B, but for the measured displacements as a function of increasing trap stiffnesses. k_{trap} = 0.05 pN/nm: 10.1 (9.6, 10.7) nm (n = 142); k_{trap} = 0.1 pN/nm: 5.7 (5.5, 6.0) nm (n = 260); k_{trap} = 0.2 pN/nm: 3.2 (3.0, 3.5) nm (n = 156); and k_{trap} = 0.3 pN/nm: 2.6 (2.4, 2.8) pN (n = 247) (source data are provided as a Source Data file). **D** Measured local stiffness of full-length KlpA and bead linkage, $k_{m\text{-}link}$ (mean ± SEM), as function of force for increasing trap stiffnesses (see "Methods" section for details underlying the stiffness calculations) (k_{trap} = 0.05 pN/nm: n_l = 142; k_{trap} = 0.1 pN/nm: n = 156; k_{trap} = 0.2 pN/nm: n = 156; k_{trap} = 0.3 pN/nm: n = 247). The solid black line shows the model fitted to all data, which considers the motor and bead-linkage as a worm-like chain (WLC) (see "Methods" section for a description of the model and parameters used for fitting) (source data are provided as a Source Data file). **E** As in B, but for the estimated load-free power strokes for the four different trap stiffnesses (see "Methods" section for a description of the calculation of the estimated load-free power strokes). Green bars indicate the mean values with 95% CIs. k_{trap} = 0.05 pN/nm: 42.9 (36.8, 49.0) nm (n = 142). k_{trap} = 0.1 pN/nm: 41.4 (36.4, 46.5) nm (n = 260); k_{trap} = 0.2 pN/nm: 41.8 (36.5, 41.0) nm (n = 156); and k_{trap} = 0.3 pN/nm: 44.5 (40.3, 49.2) pN (n = 247). Statistical significance was determined using a two-tailed unpaired Welch's t-test (ns: not significant; ***P = 0.0002) (source data are provided as a Source Data file).

the central stalk becomes irrelevant, resulting in non-processive behavior under load.

Our study also uncovers that both HSET and KlpA have the capability to oligomerize, and these multi-motor complexes show processive movement towards the minus ends of MTs (Figs. 1F, 2H and Suppl. Fig. 10). Consistent with these findings, our force measurements reveal that GFP-KlpA can oligomerize with mCherry-KlpA, leading to increased force generation (Fig. 1G, H). This cooperative behavior differs significantly from the relatively weak dependence on the number of motors observed in the processive Kinesin-1[19,36,37]. Our results suggest that the non-processive nature of Kinesin-14 motors is crucial for their cooperative ability. Motors with low duty ratios, like the non-processive ones, are less likely to interfere with the functioning of other motors compared to high duty ratio, processive motors. This is analogous to the role of non-processive myosin-2 in muscle filament sliding[46–48], suggesting that Kinesin-14 motors are evolutionarily adapted to work collectively in driving the inward-directed sliding motion of anti-parallel MTs and countering the outward-directed forces of mitotic Kinesin-5 motors, which act oppositely on the same MT pairs during metaphase[2].

Furthermore, our study shows that single HSET molecules are non-processive under load, performing single power strokes per MT encounter and generating forces of only ~0.5 pN (Fig. 2C, D). This contradicts earlier assertions of HSET's processivity and higher force generation[25]. Our experiments, including photo-bleaching (to rule out motor aggregation) and motor-dilution experiments using the optical-

https://doi.org/10.1038/s41467-024-50990-x

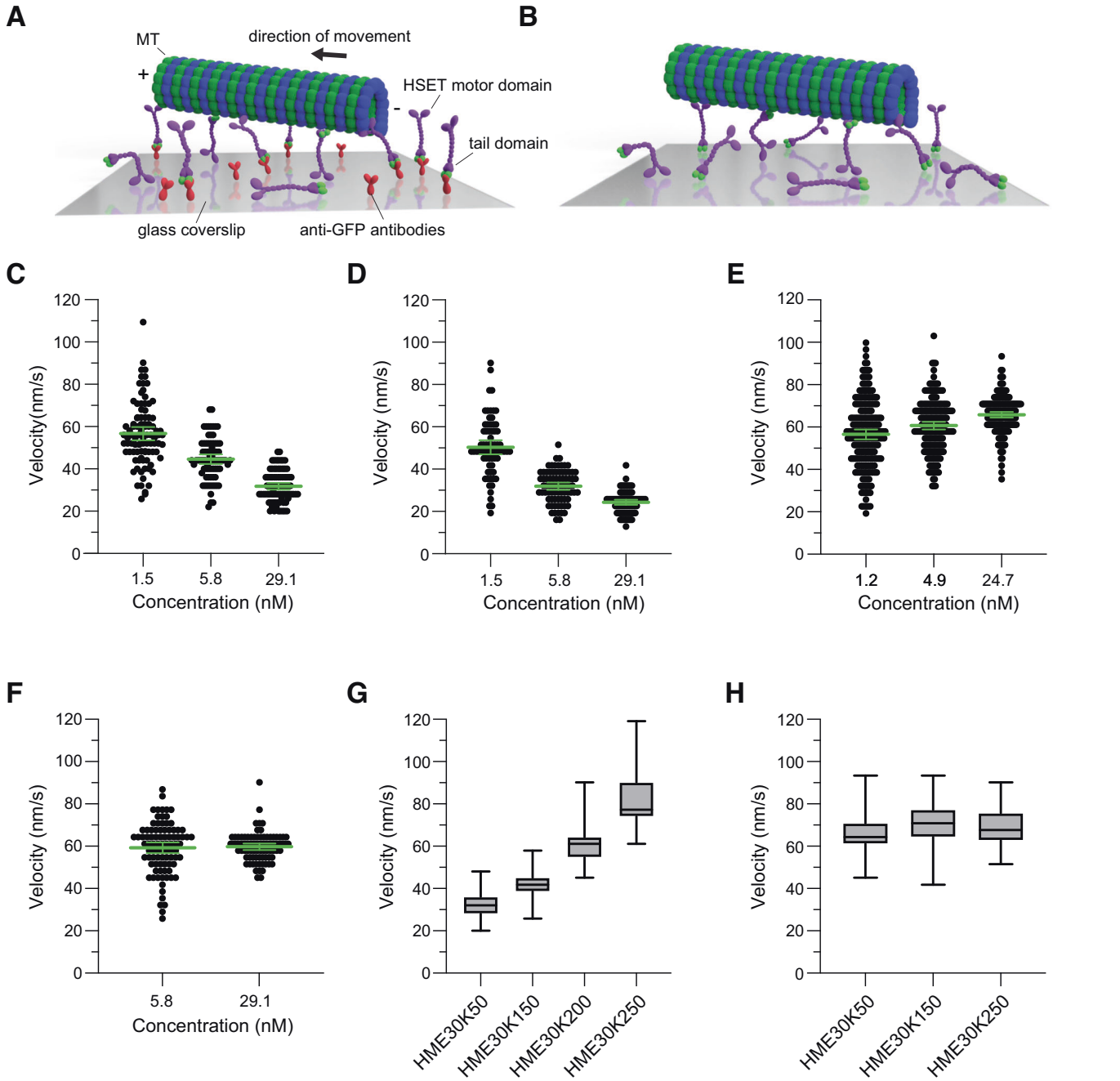

Fig. 4 | Cooperative effect of multiple HSET molecules on MT-gliding velocity. **A** MT-gliding assay: GFP-HEST bound to cover glass via anti-GFP antibodies; non-specifically bound motors interact with the gliding MT through their tails. **B** MT-gliding assay without surface-bound antibodies: motors are non-specifically absorbed to the cover glass. Increased interactions between the motor tails and the gliding MT occur due to random motor orientations. **C** MT-gliding velocities with increasing HSET concentrations bound to the cover glass via anti-GFP antibodies. Green bars represent the mean values with 95% CIs. MT-gliding velocity in HME30K50 buffer (HME30 buffer (HEPES 30 mM, pH 7.2, $MgCl_2$ 2 mM, EGTA 1 mM) with 50 mM KCl) at 1.5 nM: 56.7 ± 1.6 nm/s (n = 92); 5.8 nM: 44.7 ± 1.1 nm/s (n = 75); and 29.1 nM: 31.8 ± 0.8 nm/s (n = 81) (source data are provided as a Source Data file). **D** MT-gliding velocities for non-specifically bound HSET in HME30K50 buffer. Green bars represent the mean values with 95% CIs. 1.5 nM: 50.3 ± 1.7 nm/s (n = 69); 5.8 nM: 31.9 ± 0.9 nm/s (n = 78); and 29.1 nM: 24.3 ± 0.6 nm/s (n = 77) (source data are provided as a Source Data file). **E** MT-gliding velocities for GFP-HSETΔTail bound via anti-GFP antibodies in HME30K50 buffer. Green bars represent the mean values with 95% CIs. 1.2 nM: 56.56 ± 1.18 nm/s (n = 195); 4.9 nM: 60.72 ± 0.91 nm/s (n = 193); and 24.7 nM: 65.82 ± 0.67 nm/s (n = 176). The velocity increases are statistically significant (P = 0.0054 and P < 0.0001, two-tailed t-test) (source data are provided as a Source Data file). **F** MT-gliding velocity of HSET in HME30 buffer containing 200 mM KCl. Green bars represent the mean values with 95% CIs. 5.8 nM: 59.2 ± 1.3 nm/s (n = 88); and 29.1 nM: 59.7 ± 0.8 nm/s (n = 81) (source data are provided as a Source Data file). **G** MT-gliding velocity of HSET vs. ionic strength (HME30 buffer with varying KCl): 29.1 nM GFP-HSET. HME30K50 buffer: 31.8 ± 0.8 (mean ± SEM) nm/s (n = 81); HME30K150: 42.4 ± 0.7 nm/s (n = 81); HME30K200: 59.7 ± 0.8 nm/s (n = 81); HME30K250: 81.7 ± 1.4 nm/s (n = 83). The whiskers indicate the range from minimum to maximum values. The boxes extend from the 25th to 75th percentiles, with the middle lines indicating the median values (source data are provided as a Source Data file). **H** MT-gliding velocities of GFP-HSET-ΔTail bound to via anti-GFP antibodies vs. ionic strength (24.7 nM GFP-HSET-ΔTail): HME30K50 buffer: 65.7 ± 0.9 nm/s (mean ± SEM) (n = 99); HME30K150: 70 ± 1 nm/s (n = 102); and HME30K250: 68.8 ± 0.9 nm/s (n = 97) (source data are provided as a Source Data file).

trapping assay, reinforce the conclusion that the previously reported 1.1 pN force likely resulted from the cooperative action of multiple HSET molecules. Importantly, we verified that the expression system was not a source of error, as HSET expressed in insect cells and *E. coli* bacteria generated similar ~0.5 pN forces (Fig. 2C, D and Suppl. Fig. 22). The weak force-generation capabilities of HSET we report here is further substantiated by observations that achieving a force of approximately 1 pN necessitates the collaboration of 2-3 Ncd molecules[19].

At higher motor concentrations, we observed substantial forces up to ~8 pN for KlpA and ~4 pN for HSET. The measured forces depend on factors such as the maximum number of motors in an oligomer and the presence of motors that non-specifically bind to the bead surfaces, contributing to force generation. These forces required movements spanning over ~100 nm under load (Fig. 1G and Fig. 2I). This observation suggests that multiple KlpA and HSET molecules exhibit processive motion when working collectively. The generality of this property within the Kinesin-14 family is supported by studies on Ncd. Ncd not only generates additive forces when functioning in teams but also demonstrates processive movement under unloaded conditions when assembled in groups using DNA scaffolds[19]. Additionally, assemblies of the *Saccharomyces cerevisiae* Kinesin-14 motor Pkl1 exhibit processive motion along MTs when bound to a single quantum dot[32]. Hence, the cooperative behavior observed among non-processive Kinesin-14 motors appears to be conserved across different species.

The limited force production of Kinesin-14 motors can be explained by a cryoEM study that investigated the ATP-driven power stroke of Ncd[18]. In contrast to the processive movement of Kinesin-1, which takes ATP-hydrolysis driven hand-over-hand steps of ~8 nm along MT filaments[54], Ncd exhibits a distinct mechanism. During each encounter with a MT, Ncd's coiled-coil stalk undergoes a single ATP-driven rotation of ~70° towards the minus-end of the MTs[18]. This angular displacement can be used to relate the estimated load-free power strokes we report here to the lever-arm lengths of the motors.

Our analysis from tail-truncation experiments, integrated with motor stiffness measurements, revealed that the load-free power-stroke lengths for both full-length KlpA and HSET are in the vicinity of 35 and 31 nm, respectively. This finding is supported by predictions from AlphaFold[45], which suggest lever-arm lengths of about 32 and 25 nm for KlpA and HSET, respectively (Suppl. Fig. 14), corresponding to power stroke lengths of 39 and 31 nm when accounting for the 70° angular displacement[18] (Suppl. Fig. 23). Thus, the estimated load-free power strokes we present here for KlpA and HSET are in close agreement with the predictions from AlphaFold, suggesting that the approximation of the motor's force-dependent stiffnesses by a WLC model results in rather accurate estimation of the actual power-stroke lengths. Notably, our finding of a 32 nm lever arm means that KlpA has the largest known lever arm among molecular motors today, surpassing Myosin V, which has a lever arm length of 26 nm[55]. Interestingly, our measurements show a closer agreement for HSET, likely due to sequence variations in the coiled-coils and the resulting differences in the persistence lengths of the lever arms. Moreover, our assay-specific considerations indicate that these measurements represent the minimal detectable power-stroke sizes, considering potential bead rotation and axial position shifts during the power stroke (Suppl. Fig. 20). In addition, while we assume a 70° angular displacement that is symmetric about the optical axis of the optical trap (Suppl. Fig. 23), it is possible that the starting angle and the range of the power stroke differ between different members of the Kinesin-14 family. Finally, it is possible that other non-linear models may describe the force-dependent stiffnesses of Kinesin-14 motors more accurately than the WLC model we used here. However, we don't expect that other models will result in significantly improved estimates for the lever-arm lengths of Kinesin-14 motors as the AlphaFold predictions and our combined lever-arm truncations and optical trapping studies agree already rather well despite the possible shortcomings described above.

The discrepancy in a previous three-bead optical tweezers study of full-length Ncd (amino acids 1-700), which reported a power stroke of only ~9 nm even after compliance correction[23], likely stems from non-specific motor binding to the pedestal bead. This binding method likely rendered the measurements less sensitive to variations in tail length. Supporting this hypothesis, our measurements on a tail-truncated Ncd construct (amino acids 209-700) revealed an uncorrected power stroke of ~9 nm, in contrast to the ~6 nm reported for full-length Ncd[23]. This difference suggests that a substantial portion of the tail's coiled-coil did not contribute to the power stroke in the earlier measurements. AlphaFold's prediction of a ~ 22 nm lever arm for full-length Ncd (Suppl. Fig. 14C) and the corresponding power stroke of ~27 nm (Suppl. Fig. 23) is largely consistent with the estimated load-free power stroke of ~29 nm for a slightly shorter Ncd construct (Suppl. Figs. 14C and 18D). That our estimated load-free power stroke size for the shorter Ncd construct is somewhat larger than the power stroke size that one calculates from the predicted length of the full-length lever arm, not only underscores the importance of the length of the coiled-coil sequences but also implies that additional sequences in the unstructured tail region (amino acids 1-194 in Ncd) may also contribute to the motor's lever-arm length.

Measurements on Ncd at limiting ATP concentrations also indicated a ~2 nm axial displacement upon initial MT binding, along with a ~2 nm off-axis component[23]. In contrast, our measurements for all tested Kinesin-14 motors did not show any measurable displacements upon MT binding in the absence of ATP (Suppl. Figure 4). This discrepancy may arise from the method of attaching the MT to the trapping beads in the three-bead assay, where the MT is connected not at its ends but at sites along the MT. Such an attachment leads to MT bending when force is applied through the attached beads, potentially causing off-axis measurements and initial off-axis displacements upon motor binding. In contrast, in our single-bead assay, where the MT is attached to the cover-glass surface and the bead is directly centered on top of the MT, all three tested Kinesin-14 motors completed the power stroke in a single ATP-driven step along the MT's long axis (Fig. 1E and Suppl. Fig. 7). Therefore, for more accurate measurements of power strokes in MT-associated kinesins, the single-bead assay seems more appropriate, unless the MTs are attached end-on to the trapping beads in the three-bead assay.

Beyond resolving discrepancies from previous studies, our research reveals that the force generation of Kinesin-14 motors is limited by their ability to displace the lever arm under load and the force produced per unit of displacement. Our study demonstrates that the force output of HSET increases with trap stiffness (Suppl. Fig. 13A), while the displacement it generates decreases (Suppl. Fig. 13B). This indicates that a higher load restricts HSET's ability to complete a full power stroke, similar to an arm-wrestler facing a stronger opponent. Consequently, the finite length and load-dependency of their lever arms lead to HSET and KlpA generating an average force of merely around 0.5 pN. While it has been previously suggested that a pair of Ncd molecules is required to generate a force of about 0.5 pN[19], the lower trap stiffnesses used in this study (0.014-0.027 pN/nm) might have limited the ability to observe the full force-generation potential of individual Ncd molecules. In summary, Kinesin-14 motors, although non-processive and relatively weak in force generation when operating individually under load, display processive motion and generate substantial forces when operating collectively.

Finally, we have successfully identified the root cause of the previously observed negative cooperativity of HSET and Ncd in multi-motor assemblies during MT-gliding assays[20,31]. We discovered that this phenomenon arises from unwanted interactions between the N-terminal MT-binding tails of the Kinesin-14 motors and the transported MT, facilitated by non-specific motor interactions with the cover glass. Essentially, these interactions act as brakes, impeding the gliding motion. Confirming our hypothesis, MT-gliding assays with tail-

less variants of HSET and KlpA showed increases in velocity as the motor concentrations were raised. Thus, akin to the functioning of myosin-2 motors in muscle[46,47], Kinesin-14 motors have evolved to collaborate effectively in sliding anti-parallel MTs inward within the mitotic spindle. This cooperative behavior generates substantial forces that counterbalance the opposing forces generated by the MT plus-end-directed tetrameric Kinesin-5 motors during metaphase.

Methods

Plasmids

The pET-17b plasmid containing the codon-optimized GFP-KlpA construct is from a previous study[17]. The truncated KlpA constructs KlpA-T1 (amino acids 298-770) and KlpA-T2 (250-770) were generated using Gibson Assembly (NEB, #E5510). The mCherry-KlpA construct was derived by replacing the N-terminal GFP of GFP-KlpA with the sequence of mCherry. The full-length HEST and the tail-truncated HSET (HSETΔTail) constructs were prepared using the HSET cDNA corresponding to Gen Bank Accession Number BC121041. The full-length HSET construct (amino acids 1-673) and the HSETΔTail construct (amino acids 139-673) were fused with the N-terminal ZZ-Tev tag for purification as well as the GFP sequence for fluorescence microscopy and for binding to anti-GFP antibody-coated trapping beads. These constructs were integrated into the pFastbac vector using Gibson Assembly (NEB, #E5510) for insect-cell expression. Full-length Ncd (amino acids 1-700) and tail-truncated Ncd (NcdΔTail) were prepared using the Ncd cDNA corresponding to Gen Bank Accession Number NM_057303.5. Both constructs were then fused at the N-terminus to a His-tag for purification purposes and a GFP for TIRF microscopy and for the binding to anti-GFP antibody-coated trapping beads.

Protein expression and purification from E. *coli*

GFP-KlpA, KlpA-T1, KlpA-T2, mCherry-KlpA, GFP-Ncd and NcdΔTail were expressed in *E. coil* cells[56,57]. Briefly, plasmids were transformed into BL21-CodonPlus (DE3)-RIPL competent cells (Agilent Technologies, #230280) with heat shock at 42 °C for 45 s followed by recovery at 37 °C for 1 h in SOC medium. The cells were then plated onto Luria-Bertani (LB) agar plate containing 50 μg/mL ampicillin and 30 μg/mL chloramphenicol. Subsequently, a single colony was carefully selected and inoculated in 3 mL of LB broth for optimal growth. The 3-mL culture was incubated at 37 °C overnight with continuous shaking. It was then used to inoculate 400 mL of LB broth supplemented with 50 μg/mL ampicillin and 30 μg/mL chloramphenicol. The 400-mL culture was incubated at 37 °C with vigorous shaking for 4-5 h and subsequently cooled on ice for 1 h. To induce expression, isopropyl β- d-1-thiogalactopyranoside (IPTG) was added to the culture at a final concentration of 0.1 mM. For the expression of GFP-KlpA, KlpA-T1, KlpA-T2, and mCherry-KlpA, the culture was shaken at 18 °C overnight. For the expression of GFP-Ncd and NcdΔTail, the culture was shaken at 18 °C for only 4 h to minimize protein degradation. The cells were harvested by centrifugation at 3000 × *g* for 10 minutes at 4 °C. Following the removal of the supernatant, the cell pellet was fully resuspended in 5 mL of B-PER complete bacterial protein extraction reagent (Thermo Fisher Scientific, #89821) containing 2 mM $MgCl_2$, 1 mM EGTA, 1 mM DTT, 0.1 mM ATP, 2 mM PMSF, and 10% glycerol. The fully resuspended cells were flash-frozen and stored at -80 °C for further use.

The frozen cells were thawed at 37 °C. Following thawing, the solution was nutated at room temperature for 20 minutes to allow the lysozyme in the B-PER extraction reagent-containing solution to lyse the cells. The cells were then further lysed by douncing on ice with 10 strokes. The resulting cell lysate was clarified by centrifugation at 265,000 × *g* for 10 minutes at 4 °C using a TLA-110 rotor in a Beckman Coulter tabletop ultracentrifuge unit. The lysate supernatant was mixed with 200 μL of Ni-nitrilotriacetic acid (Ni-NTA) resin (Roche Complete His-Tag purification resin, MilliporeSigma, #5893682001) and incubated at 4 °C with gentle nutation for 1 h. Afterwards, the resin was washed with wash buffer (50 mM HEPES, 300 mM KCl, 2 mM $MgCl_2$, 1 mM EGTA, 1 mM DTT, 1 mM PMSF, 0.1 mM ATP, 0.1% Triton X-100, 10% glycerol, pH 7.2). Then, the protein was eluted using elution buffer (wash buffer with 250 mM imidazole). The eluate was flash-frozen and stored at -80 °C for further use.

Protein expression and purification from insect cells

HSET and HSETΔTail were expressed in Sf9 cells (Gibco, #11496015)[56]. Briefly, the pFastBac plasmid containing either HSET or HSETΔTail was transformed into DH10Bac-competent cells (Gibco, #10361012) by subjecting the cells to heat shock at 42 °C for 45 s, followed by recovery at 37 °C for 4 h in S.O.C. medium (Gibco, #15544034). Subsequently, the transformed cells were plated onto LB agar plates supplemented with kanamycin (50 μg/mL), gentamicin (7 μg/mL), tetracycline (10 μg/mL), BluoGal (100 μg/mL), and IPTG (40 μg/mL). After a 36-h incubation period, positive clones were identified based on the blue/white color screen. Subsequently, a single white colony was carefully selected and inoculated in 3 mL LB broth supplemented with kanamycin (50 μg/mL), gentamicin (7 μg/mL), tetracycline (10 μg/mL) followed by incubation at 37 °C overnight. Bacmid DNA was extracted from overnight culture using an isopropanol precipitation method with Qiagen buffer (Qiagen, #27104)[56]. For the generation of baculovirus intended for Sf9 insect cell transfection, 2 mL of Sf9 cells at a density of 0.5×10^6 cells per mL were seeded into six-well plates (Corning, #3516). Subsequently, transfection was carried out by adding 2 μg of freshly prepared bacmid DNA and 6 μL of FuGene HD transfection reagent (Promega, #E2311), following the instructions provided by the manufacturer. The cells were incubated for 4 days, and the supernatant containing P0 virus was collected. To generate P1 virus, 0.5 mL of P0 virus was used to transfect 50 mL of Sf9 cells at 1.5×10^6 cells per mL. The supernatant containing P1 virus was collected by centrifugation at 200 × *g* for 5 minutes at 4 °C after 3 days. The P1 virus was stored at 4 °C in the dark until use. To initiate protein expression, 5 mL of the P1 virus was utilized to transfect 500 mL of Sf9 cells at a density of 2×10^6 cells per mL. Following a 60-h incubation period, the cells were harvested by centrifugation at 3000 × g for 10 minutes at 4 °C. The resulting cell pellet was resuspended in 15 mL of ice-cold PBS and subjected to another round of centrifugation. After removing the supernatant, the cell pellet was flash-frozen in liquid nitrogen and stored at -80 °C for subsequent use.

HSET and HSETΔTail were purified from frozen Sf9 pellets[56]. The frozen pellets from a 500-mL insect cell culture were thawed on ice and resuspended in lysis buffer (50 mM HEPES, pH 7.4, 2 mM $MgCl_2$, 1 mM EGTA, 100 mM NaCl, 1 mM DTT, 0.1 mM ATP, 10% [v/v] glycerol, 2 mM PMSF) supplemented with one protease inhibitor cocktail tablet (cOmplete-EDTA free, Roche, #11836170001) to a final volume of 50 mL. The cells were lysed using a dounce homogenizer with 20 strokes, and the resulting lysate was cleared by centrifugation at 265,000 × *g* for 10 minutes at 4 °C using a TLA-110 rotor in a Beckman Coulter tabletop ultracentrifuge unit. The clarified supernatant was incubated with 3 mL of IgG Sepharose 6 Fast Flow beads (Cytiva, #17096901) for 4 h with rotation. Following the incubation period, the protein-bound IgG beads were transferred to a gravity flow column. The beads were then washed sequentially with 100 mL of lysis buffer and 100 mL of TEV buffer (50 mM Tris–HCl, pH 8.0, 250 mM KAc, 2 mM $MgCl_2$, 1 mM EGTA, 1 mM DTT, 0.1 mM Mg-ATP and 10% [v/v] glycerol). Subsequently, the beads were resuspended in TEV buffer with a final volume of 5 mL. Then, 100 μL of TEV protease (New England Biolabs, #P8112S) was added, and the mixture was incubated at 4 °C on a roller overnight. After TEV cleavage, the beads were separated by centrifugation at 1000 × *g* for 1 minute at 4 °C, and the protein of interest was concentrated to 1 mL using a 50 kDa

molecular weight cut-off (MWCO) centrifugal filter (Millipore, #UFC505024). Finally, the concentrated protein was flash-frozen in liquid nitrogen for storage.

Polymerization of polarity-marked MTs

Polarity-marked MTs were polymerized from tubulins[58]. Briefly, unlabeled porcine brain tubulin (Cytoskeleton, #TL590M), biotin-tagged tubulin (Cytoskeleton, #T333P) and rhodamine-labeled tubulin (Cytoskeleton, #T240) were dissolved in buffer (80 mM PIPES, 2 mM $MgCl_2$, 1 mM EGTA, 10% glycerol, 1 mM DTT, 1 mM GTP) to a final concentration of 2 mg/mL. To create the brighter MT ends ("the seeds"), 0.3 µL of each tubulin was mixed and then incubated at 37 °C for 5 min. 6 µL of unlabeled tubulin, 0.3 µL of biotin-tagged tubulin, and 0.3 µL of rhodamine-labeled tubulin were added to this mixture, followed by a further 20-minute incubation at 37 °C. Subsequently, paclitaxel was added to the mixture to reach a final concentration of 1 mM, and the mixture was incubated for an additional 10 minutes at 37 °C. To remove un-incorporated tubulin, the tubulin mixture was carefully layered over a 60-µL glycerol cushion (80 mM PIPES, 2 mM $MgCl_2$, 1 mM EGTA, 1 mM DTT, 10 µM paclitaxel, and 60% glycerol) and centrifuged at 280,000 × *g*) for 10 minutes at room temperature using a TLA-100 rotor in a Beckman Coulter tabletop ultracentrifuge unit. Following the centrifugation, the supernatant was removed and the pellet was washed twice by pipetting 20 µL buffer (80 mM PIPES, 2 mM $MgCl_2$, 1 mM EGTA, 1 mM DTT, 10 µM paclitaxel, and 10% glycerol) onto the pellet, followed by immediate removal of the buffer. Finally, the pellet was resuspended in 7.5 µL buffer (80 mM PIPES, 2 mM $MgCl_2$, 1 mM EGTA, 1 mM DTT, 10 µM paclitaxel, and 10% glycerol) by gentle pipetting. The final MT stock solution was stored at room temperature in the dark and used within 2 days.

MT-binding and -release assay

MT-binding and -release purification was performed to further purify the motor proteins and to remove any inactive motors and aggregates. 50 µL of purified protein was buffer exchanged into low-salt buffer (30 mM HEPES, pH 7.2, 50 mM KCl, 2 mM $MgCl_2$, 1 mM EGTA, 1 mM DTT, and 0.1 mM AMPPNP) using a 0.5-mL Zeba spin desalting column (7-kD molecular weight cutoff, Thermo Fisher Scientific, #89882). AMP-PNP and paclitaxel were added to the flow-through to final concentrations of 1 mM and 10 µM, respectively. After adding 5 µL of 5 mg/mL paclitaxel-stabilized MTs to the mixture, the solution was incubated at room temperature for 5 minutes to allow motors to bind to the MTs. The mixture was centrifuged through a 100-µL glycerol cushion (80 mM PIPES, 2 mM $MgCl_2$, 1 mM EGTA, 1 mM DTT, 10 µM paclitaxel, and 60% glycerol) at 60,000 × *g* for 10 minutes at room temperature using a TLA-100 rotor in a Beckman Coulter tabletop ultracentrifuge unit. Subsequently, the supernatant was carefully removed, and the pellet was resuspended in 50 µL of high-salt buffer (30 mM Hepes, 300 mM KCl, 2 mM $MgCl_2$, 1 mM EGTA, 1 mM DTT, 10 µM paclitaxel, 3 mM ATP, and 10% glycerol). The MTs were separated by centrifugation at 60,000 × *g* for 5 minutes at room temperature. The resulting supernatant, namely the MT-release (MT-R) fraction, was collected and divided into aliquots. The aliquots were then flash-frozen in liquid nitrogen and stored at -80 °C for further use.

MT-gliding assay

The flow chamber was assembled using a cleaned coverslip, a glass slide, and two stripes of parafilms[59]. To immobilize motors on the coverslip surface, 12 µL of a 0.4 mg/mL rabbit monoclonal anti-GFP antibody solution was introduced into the slide chamber and incubated for 10 min. The chamber was then washed twice with 20 µL of blocking buffer (80 mM PIPES, 2 mM $MgCl_2$, 1 mM EGTA, 1% Pluronic F-127, and 1 mg/mL α-casein). The blocking buffer was incubated for an additional 10 minutes to block the glass surface. After the blocking step, the slide chamber was washed twice with 20 µL motility buffer (HEPES 30 mM, pH 7.2, $MgCl_2$ 2 mM, EGTA 1 mM, with appropriate KCl concentration). Subsequently, 10 µL of the motor solution (appropriately diluted in motility buffer) was introduced into the slide chamber and incubated for 2 min. The flow chamber was then washed twice with 20 µL motility buffer to remove unbound motors. A final 20 µL motility buffer containing fluorescently labeled MTs and supplied with 1 mM ATP, 20 µM paclitaxel, 50 mM glucose, and 1 µL of oxygen scavenger system (gloxy) was introduced into the chamber. MTs were visualized and imaged with an acquisition time of 200 ms for a total of 200 frames per movie with a commercial total internal reflection fluorescence (TIRF) microscope (Cairn and BioVision). The velocity was analyzed using Fiji (ImageJ2), and the statistical analysis and data visualization were performed using GraphPad Prism (version 10).

Optical tweezers assay

Force measurements using optical tweezers were conducted with a LUMICKS' C-Trap combined with TIRF and interference reflection microscopy (IRM). The slide chamber assembly and polarity-marked MTs were prepared as described in sections "MT-gliding assay" and "Polymerization of polarity-marked MTs"[38]. The polarity-marked, rhodamine X-labeled, and biotinylated MTs were immobilized onto a glass coverslip using α-casein-biotin and streptavidin. For single-molecule level measurements, each motor protein was appropriately diluted in motility buffer (30 mM HEPES, 50 mM KAc, 2 mM $MgCl_2$, 1 mM EGTA, 1 mM DTT, 10 µM paclitaxel, 50 mM glucose, gloxy, 0.75 mg/mL α-casein, 0.25% Pluronic F-127, pH 7.2) and incubated with anti-GFP antibody-coated beads (~1 µm in diameter; carboxyl-modified polystyrene microspheres, Polysciences, #08226-15) for 10 min. The mixture was then supplemented with 1 mM ATP and introduced into the slide chamber. Trapping assays were performed at 25 °C, using trap stiffnesses ranging from 0.05 to 0.3 pN/nm. For force measurements involving multi-motor KlpA complexes, anti-GFP antibody-coated beads were initially incubated with GFP-tagged KlpA at single-molecule concentrations for 10 minutes on ice. Following this, the beads were centrifuged at 1000 × *g* for 2 min, and the supernatant was carefully removed. The beads were then resuspended in 10 µL of motility buffer containing appropriately diluted mCherry-tagged KlpA and incubated on ice for an additional 5 min. After a second centrifugation at 1000 × *g* for 2 minutes and the subsequent removal of the supernatant, the beads were resuspended in 40 µL of motility buffer supplemented with 1 mM ATP and then introduced into the chamber. While some residual mCherry-tagged motors remain in solution following this procedure, these motors do not accumulate on the MTs due to their brief, non-processive power strokes (Suppl. Fig. 5B). Therefore, the residual motors will not affect the bead-based force measurements, except through their binding to the trapping beads. This binding would enhance the force measurements rather than negatively impact them.

Analysis of optical trapping data

The optical trapping data were initially sampled at a rate of 20 MHz and then digitally down-sampled by a factor of 256, resulting in a final sample rate of 78.125 kHz. An anti-aliasing filter was applied to achieve a passband of 31.25 kHz, and the resulting data were fitted to the Lorentzian power spectrum. The data, sampled at 78.125 kHz, were then transferred to a secure data server, and subsequently processed using a custom-written MATLAB program. Within this program, an averaging window spanning 200 data points was applied to the data for visualization, serving to reduce noise while retaining the key features of the data. Motor-MT interactions were identified by a noticeable decrease in noise within the z-signal (Suppl. Figure 4), indicative of motor binding to the MT. A binding event was classified as a power stroke if it resulted in an average displacement of ~2 nm or more, aligning with the detection limit of our measurements. To quantify the power-stroke magnitude and associated force, we placed the

positional markers to the initiation and termination points of the displacement deviation (Suppl. Fig. 24). This positioning automatically triggered the calculation of the average distance from the trapping center (indicating the power-stroke size), the variance in position during the post-power stroke phase (to calculate the motor's compliance), and the corresponding force generated, using the non-averaged data.

Calculation of the compliance of the motor- and GFP-antibody bead linkage and correction of the power stroke

The motor and the GFP-antibody bead linkage together create a series compliance with the bead. Consequently, the measured bead displacement during the motor's power stroke is smaller than the actual motor displacement, behaving like springs under load. To estimate the compliance-corrected motor displacement, we analyzed the variance $\sigma^2(x_b)$ of the bead's position under a force produced during a power stroke. This method, previously applied to kinesin-1 stepping along MTs in a stationary optical trap[53,60], is based on the equipartition theorem and assumes a linear force-extension relation for the elastic elements with force-independent stiffnesses. The combined stiffness of the motor and bead-linkage, $k_{\text{m-link}}$, is defined by:

$$k_{\text{m-link}} = \frac{k_B T}{\sigma^2(x_b)} - k_{\text{trap}}. \tag{1}$$

Given that $k_{\text{m-link}}$ accounts for various unknown elastic elements and fluctuations, we anticipated its dependency on force. We, therefore, consider $k_{\text{m-link}}$ as a local property in the vicinity of a given force and refer to it as a local stiffness. To determine the force-dependent stiffness, we measured the variance of the trapped bead during each power stroke. The trap stiffness k_{trap} derived from the optical trap's active calibration[61] accounts for processes such as parasitic filtering of the position-sensitive detector (PSD)[62]. The variance analysis does not consider these processes; hence, we compared the variance of the trapped bead during the power stroke to the baseline position variance before and after the power stroke. These variance values were then used to calculate $k_{\text{m-link}}$. The calculated $k_{\text{m-link}}$ values were subsequently smoothened using a sliding window of 0.1 pN width (see, for example, Fig. 3D).

The observed increase in the local stiffness with force suggests a non-linear elasticity of the bead's linkage to the filament. To determine the relation between the compliance-corrected motor displacement and the measured bead position for a given trap stiffness, we used the worm-like chain (WLC) model. This model describes the non-linear elasticity of biological polymers, including DNA[41] and proteins[42–44]. The WLC force-extension relation is approximated as[63]:

$$F_{\text{WLC}}(x_b) = \frac{kT}{l_p}\left(\frac{1}{4}\left(1 - \frac{(x_m - x_b)}{L_0}\right)^{-2} - \frac{1}{4} + \frac{(x_m - x_b)}{L_0}\right), \tag{2}$$

where L_0 is the contour length and l_p is the persistence length. Both parameters are free fit parameters in our model. This approach treats the motor's three-dimensional geometry with its lever arm as a one-dimensional problem, combining effects from bending and stretching of the lever arm and motor domain into one non-linear force-extension relation. Consequently, it is challenging to relate the contour length and the persistence length obtained from the WLC model to the physical length scales of the motor protein's lever arm.

The potential energy of the trapped bead is defined by the quadratic potential from the optical trap and the non-linear potential from the WLC as:

$$V(x_b) = \frac{k_{trap}}{2} x_b^2 - \int F_{\text{WLC}} dx_b. \tag{3}$$

This integral can be solved analytically. Assuming mechanical equilibrium, the variance is given by:

$$\sigma^2(x_b) = \langle x_b^2 \rangle - \langle x_b \rangle^2 = \int_{-\infty}^{\infty} x_b^2 P(x_b) dx_b - \left(\int_{-\infty}^{\infty} x_b P(x_b) dx_b \right)^2 \tag{4}$$

where $P(x_b)$ is the normalized Boltzmann distribution:

$$P(x_b) = \frac{e^{-V(x_b)/kT}}{\int e^{-V(x_b)/kT} dx_b}. \tag{5}$$

These integrals are numerically solvable, and we implemented their solution into a fitting procedure that minimizes the squared distance between the model's local stiffness and the experimentally obtained local stiffness. We used Python's numpy and scipy packages for minimization and integration. For the unknown motor position x_m (i.e., the proximal end of the lever arm), we used a range from 1 to 120 nm. Including variance measurements for low forces (<0.2 pN) resulted in unrealistic large estimated motor displacements (>70 nm). We reasoned that a hinge-like flexibility of the lever arm at low forces could contribute to the variance, and that the variances above 0.2 pN more faithfully reflect the elasticity of the coiled-coil lever arm. To address this, we introduced the lower-bound $k^{\text{min}}_{\text{m-link}} = 0.01\,\text{pN/nm}$ for the local stiffness for all constructs. This lower bound defines the stiffness of the WLC for small forces and provides a constraint between the two free parameters:

$$l_p = \frac{3kT}{2L_o k^{\text{min}}_{\text{m-link}}} \tag{6}$$

By using this constraint, the WLC model was reduced to a single free model parameter, L_0, resulting in a very robust fitting procedure. The results of these fits (KlpA: $L_0 = 77.59$ nm; HSET: $L_0 = 89.39$ nm; Ncd: $L_0 = 67.05$ nm; KlpA-T1: $L_0 = 71.89$ nm) are shown in Fig. 3D and Supplementary Figs. S13C, S16C, and S18C. Atomic force microscopy measurements[64] suggests that the contour lengths of the coiled-coils of 223 residues (KlpA), 169 residues (HSET), 151 residues (Ncd), and 110 residues (KlpA-T1) (Suppl. Fig. 14A) are approximately 80, 60, 55, and 40 nm (0.36 nm per residue[64]), respectively, when the coiled-coils are stretched. While the chosen $k^{\text{min}}_{\text{m-link}}$ is extrapolated and we propose that Kinesin-14's coiled-coils bend under load rather than being stretched, the reported measurements suggest that the contour lengths we obtain from our WLC model may be close to the true contour lengths of Kinesin-14's lever arms even under bending.

With the calibrated WLC model, we could numerically invert the functions to determine the corrected motor position x_m for a bead displacement at a given trap stiffness, which we then interpret as an estimate for the load-free power stroke. We calculated the error range for the estimated load-free power strokes by performing two additional fits of the WLC model to the local stiffness data: one by adding the associated SEM to the stiffness data and another by subtracting the SEM. These fits provided the upper and lower bounds of the estimated load-free power strokes. We used these bounds to calculate single value errors, termed "propagated error", by determining the difference between the value of the mean and the upper and lower bounds, then choosing then the larger difference as the presented error of the mean.

Finally, to compare the estimated load-free power stroke length with the power stroke length predicated by AlphaFold (Suppl. Fig. 23), we adjusted for the length of the GFP-antibody bead linkage by subtracting 8 nm. This adjustment accounts for the 4-nm length of GFP and a part of the ~8-nm-long antibody complex (Suppl. Fig. 25). The antibody's heavy chains are ~8.5 nm long, with about half of this length forming the variable light chains[65]. Depending on which part

of the entire antibody complex adheres to the bead surface during the cross-linking process, we estimate that approximately 8 nm effectively contributes to the length of the GFP-antibody bead linkage once the GFP is bound to the antigen-binding sites (Suppl. Fig. 25).

Reporting summary

Further information on research design is available in the Nature Portfolio Reporting Summary linked to this article.

Data availability

Data supporting the findings of this manuscript are available from the corresponding author upon request. Source data are provided with this paper.

References

1. Walczak, C. E. & Heald, R. Mechanisms of mitotic spindle assembly and function. *Int. Rev. Cytol.* **265**, 111–158 (2008).
2. Peterman, E. J. & Scholey, J. M. Mitotic microtubule crosslinkers: insights from mechanistic studies. *Curr. Biol.* **19**, R1089–R1094 (2009).
3. Cross, R. A. & McAinsh, A. Prime movers: the mechanochemistry of mitotic kinesins. *Nat. Rev. Mol. Cell Biol.* **15**, 257–271 (2014).
4. Pandey, H., Popov, M., Goldstein-Levitin, A. & Gheber, L. Mechanisms by which kinesin-5 motors perform their multiple intracellular functions. *Int J. Mol. Sci.* **22**, 6420 (2021).
5. Mann, B. J. & Wadsworth, P. Kinesin-5 regulation and function in mitosis. *Trends Cell Biol.* **29**, 66–79 (2019).
6. Kashina, A. S., Scholey, J. M., Leszyk, J. D. & Saxton, W. M. An essential bipolar mitotic motor. *Nature* **384**, 225 (1996).
7. Scholey, J. E., Nithianantham, S., Scholey, J. M. & Al-Bassam, J. Structural basis for the assembly of the mitotic motor Kinesin-5 into bipolar tetramers. *Elife* **3**, e02217 (2014).
8. She, Z. Y. & Yang, W. X. Molecular mechanisms of kinesin-14 motors in spindle assembly and chromosome segregation. *J. Cell Sci.* **130**, 2097–2110 (2017).
9. Yamada, M., Tanaka-Takiguchi, Y., Hayashi, M., Nishina, M. & Goshima, G. Multiple kinesin-14 family members drive microtubule minus end-directed transport in plant cells. *J. Cell Biol.* **216**, 1705–1714 (2017).
10. Hepperla, A. J. et al. Minus-end-directed Kinesin-14 motors align antiparallel microtubules to control metaphase spindle length. *Dev. Cell* **31**, 61–72 (2014).
11. Cai, S., Weaver, L. N., Ems-McClung, S. C. & Walczak, C. E. Kinesin-14 family proteins HSET/XCTK2 control spindle length by cross-linking and sliding microtubules. *Mol. Biol. Cell* **20**, 1348–1359 (2009).
12. Olmsted, Z. T., Colliver, A. G., Riehlman, T. D. & Paluh, J. L. Kinesin-14 and kinesin-5 antagonistically regulate microtubule nucleation by gamma-TuRC in yeast and human cells. *Nat. Commun.* **5**, 5339 (2014).
13. Kim, N. & Song, K. KIFC1 is essential for bipolar spindle formation and genomic stability in the primary human fibroblast IMR-90 cell. *Cell Struct. Funct.* **38**, 21–30 (2013).
14. Zhu, C. et al. Functional analysis of human microtubule-based motor proteins, the kinesins and dyneins, in mitosis/cytokinesis using RNA interference. *Mol. Biol. Cell* **16**, 3187–3199 (2005).
15. Hatsumi, M. & Endow, S. A. Mutants of the microtubule motor protein, nonclaret disjunctional, affect spindle structure and chromosome movement in meiosis and mitosis. *J. Cell Sci.* **101**, 547–559 (1992).
16. Acilan, C. & Saunders, W. S. A tale of too many centrosomes. *Cell* **134**, 572–575 (2008).
17. Popchock, A. R. et al. The mitotic kinesin-14 KlpA contains a context-dependent directionality switch. *Nat. Commun.* **8**, 13999 (2017).
18. Endres, N. F., Yoshioka, C., Milligan, R. A. & Vale, R. D. A lever-arm rotation drives motility of the minus-end-directed kinesin Ncd. *Nature* **439**, 875–878 (2006).
19. Furuta, K. et al. Measuring collective transport by defined numbers of processive and nonprocessive kinesin motors. *Proc. Natl Acad. Sci. USA* **110**, 501–506 (2013).
20. Braun, M. et al. Changes in microtubule overlap length regulate kinesin-14-driven microtubule sliding. *Nat. Chem. Biol.* **13**, 1245–1252 (2017).
21. Norris, S. R. et al. Microtubule minus-end aster organization is driven by processive HSET-tubulin clusters. *Nat. Commun.* **9**, 2659 (2018).
22. Wendt, T. G. et al. Microscopic evidence for a minus-end-directed power stroke in the kinesin motor ncd. *EMBO J.* **21**, 5969–5978 (2002).
23. deCastro, M. J., Fondecave, R. M., Clarke, L. A., Schmidt, C. F. & Stewart, R. J. Working strokes by single molecules of the kinesin-related microtubule motor ncd. *Nat. Cell Biol.* **2**, 724–729 (2000).
24. Endow, S. A. & Higuchi, H. A mutant of the motor protein kinesin that moves in both directions on microtubules. *Nature* **406**, 913–916 (2000).
25. Reinemann, D. N., Norris, S. R., Ohi, R. & Lang, M. J. Processive kinesin-14 HSET exhibits directional flexibility depending on motor traffic. *Curr. Biol.* **28**, 2356–2362.e5 (2018).
26. Wang, P. et al. The central stalk determines the motility of mitotic kinesin-14 homodimers. *Curr. Biol.* **28**, 2302–2308.e3 (2018).
27. Yun, M. et al. Rotation of the stalk/neck and one head in a new crystal structure of the kinesin motor protein, Ncd. *EMBO J.* **22**, 5382–5389 (2003).
28. Nitzsche, B. et al. Working stroke of the kinesin-14, ncd, comprises two substeps of different direction. *Proc. Natl Acad. Sci. USA* **113**, E6582–E6589 (2016).
29. Kozielski, F., De Bonis, S., Burmeister, W. P., Cohen-Addad, C. & Wade, R. H. The crystal structure of the minus-end-directed microtubule motor protein ncd reveals variable dimer conformations. *Structure* **7**, 1407–1416 (1999).
30. Sablin, E. P. et al. Direction determination in the minus-end-directed kinesin motor ncd. *Nature* **395**, 813–816 (1998).
31. Kaneko, T. et al. Different motilities of microtubules driven by kinesin-1 and kinesin-14 motors patterned on nanopillars. *Sci. Adv.* **6**, eaax7413 (2020).
32. Furuta, K., Edamatsu, M., Maeda, Y. & Toyoshima, Y.Y. Diffusion and directed movement: in vitro motile properties of fission yeast kinesin-14 Pkl1. *J. Biol. Chem.* **283**, 36465–36473 (2008).
33. Allersma, M. W., Gittes, F., deCastro, M. J., Stewart, R. J. & Schmidt, C. F. Two-dimensional tracking of ncd motility by back focal plane interferometry. *Biophys. J.* **74**, 1074–1085 (1998).
34. Butterfield, A. E., Stewart, R. J., Schmidt, C. F. & Skliar, M. Bidirectional power stroke by ncd kinesin. *Biophys. J.* **99**, 3905–3915 (2010).
35. Brenner, S., Berger, F., Rao, L., Nicholas, M. P. & Gennerich, A. Force production of human cytoplasmic dynein is limited by its processivity. *Sci. Adv.* **6**, eaaz4295 (2020).
36. Elshenawy, M. M. et al. Cargo adaptors regulate stepping and force generation of mammalian dynein-dynactin. *Nat. Chem. Biol.* **15**, 1093–1101 (2019).
37. Jamison, D. K., Driver, J. W., Rogers, A. R., Constantinou, P. E. & Diehl, M. R. Two kinesins transport cargo primarily via the action of one motor: implications for intracellular transport. *Biophys. J.* **99**, 2967–2977 (2010).
38. Budaitis, B. G. et al. Pathogenic mutations in the kinesin-3 motor KIF1A diminish force generation and movement through allosteric mechanisms. *J. Cell Biol.* **220**, e202004227 (2021).
39. Svoboda, K. & Block, S. M. Force and velocity measured for single kinesin molecules. *Cell* **77**, 773–784 (1994).

40. Lam, A. J. et al. A highly conserved 310 helix within the kinesin motor domain is critical for kinesin function and human health. *Sci. Adv.* **7**, eabf1002 (2021).
41. Wang, M. D., Yin, H., Landick, R., Gelles, J. & Block, S. M. Stretching DNA with optical tweezers. *Biophys. J.* **72**, 1335–1346 (1997).
42. Minajeva, A., Kulke, M., Fernandez, J. M. & Linke, W. A. Unfolding of titin domains explains the viscoelastic behavior of skeletal myofibrils. *Biophys. J.* **80**, 1442–1451 (2001).
43. Sun, Y. L., Luo, Z. P., Fertala, A. & An, K. N. Direct quantification of the flexibility of type I collagen monomer. *Biochem. Biophys. Res. Commun.* **295**, 382–386 (2002).
44. Bustamante, C. J., Kaiser, C. M., Maillard, R. A., Goldman, D. H. & Wilson, C. A. Mechanisms of cellular proteostasis: insights from single-molecule approaches. *Annu. Rev. Biophys.* **43**, 119–140 (2014).
45. Jumper, J. et al. Highly accurate protein structure prediction with AlphaFold. *Nature* **596**, 583–589 (2021).
46. Plotnikov, S. V., Millard, A. C., Campagnola, P. J. & Mohler, W. A. Characterization of the myosin-based source for second-harmonic generation from muscle sarcomeres. *Biophys. J.* **90**, 693–703 (2006).
47. Llewellyn, M. E., Barretto, R. P., Delp, S. L. & Schnitzer, M. J. Minimally invasive high-speed imaging of sarcomere contractile dynamics in mice and humans. *Nature* **454**, 784–788 (2008).
48. Spudich, J. A. Hypertrophic and dilated cardiomyopathy: four decades of basic research on muscle lead to potential therapeutic approaches to these devastating genetic diseases. *Biophys. J.* **106**, 1236–1249 (2014).
49. Matusovsky, O. S., Mansson, A. & Rassier, D. E. Cooperativity of myosin II motors in the non-regulated and regulated thin filaments investigated with high-speed AFM. *J. Gen. Physiol.* **155**, e202213190 (2023).
50. Hentrich, C. & Surrey, T. Microtubule organization by the antagonistic mitotic motors kinesin-5 and kinesin-14. *J. Cell Biol.* **189**, 465–480 (2010).
51. Siddiqui, N. et al. Force generation of KIF1C is impaired by pathogenic mutations. *Curr. Biol.* **32**, 3862–3870.e6 (2022).
52. Shimamoto, Y., Forth, S. & Kapoor, T. M. Measuring pushing and braking forces generated by ensembles of kinesin-5 crosslinking two microtubules. *Dev. Cell* **34**, 669–681 (2015).
53. Svoboda, K., Schmidt, C. F., Schnapp, B. J. & Block, S. M. Direct observation of kinesin stepping by optical trapping interferometry. *Nature* **365**, 721–727 (1993).
54. Yildiz, A., Tomishige, M., Vale, R. D. & Selvin, P. R. Kinesin walks hand-over-hand. *Science* **303**, 676–678 (2004).
55. Sun, Y. & Goldman, Y. E. Lever-arm mechanics of processive myosins. *Biophys. J.* **101**, 1–11 (2011).
56. Fu, X. et al. Doublecortin and JIP3 are neural-specific counteracting regulators of dynein-mediated retrograde trafficking. *Elife* **11**, e82218 (2022). 11.
57. Pant, D. C. et al. ALS-linked KIF5A DeltaExon27 mutant causes neuronal toxicity through gain-of-function. *EMBO Rep.* **23**, e54234 (2022).
58. Liu, X., Rao, L. & Gennerich, A. Measurements of the force-dependent detachment rates of cytoplasmic dynein from microtubules. *Methods Mol. Biol.* **2623**, 221–238 (2023).
59. Liu, X., Rao, L. & Gennerich, A. The regulatory function of the AAA4 ATPase domain of cytoplasmic dynein. *Nat. Commun.* **11**, 5952 (2020).
60. Coppin, C. M., Pierce, D. W., Hsu, L. & Vale, R. D. The load dependence of kinesin's mechanical cycle. *Proc. Natl Acad. Sci. USA* **94**, 8539–8544 (1997).
61. Tolić-Nørrelykke, S. et al. Calibration of optical tweezers with positional detection in the back focal plane. *Rev. Sci. Instrum.* **77**, 103101 (2006).
62. Huisstede, J. H., van Rooijen, B. D., van der Werf, K. O., Bennink, M. L. & Subramaniam, V. Dependence of silicon position-detector bandwidth on wavelength, power, and bias. *Opt. Lett.* **31**, 610–612 (2006).
63. Marko, J. F. & Siggi, E. D. Stretching DNA. *Macromolecules* **28**, 8759–8770 (1995).
64. Root, D. D., Yadavalli, V. K., Forbes, J. G. & Wang, K. Coiled-coil nanomechanics and uncoiling and unfolding of the superhelix and alpha-helices of myosin. *Biophys. J.* **90**, 2852–2866 (2006).
65. Bagci, H., Kohen, F., Kuscuoglu, U., Bayer, E. A. & Wilchek, M. Monoclonal anti-biotin antibodies simulate avidin in the recognition of biotin. *FEBS Lett.* **322**, 47–50 (1993).

Acknowledgements

The authors would like to thank J. Vanlier and S. Weisenburger from LUMICKS for their helpful discussions on active trap calibration. X. Liu was supported by National Institutes of Health grants R01GM098469 and R01GM127922. L. Rao and A. Gennerich were supported by National Institutes of Health grants R01GM098469 and R01NS114636. W. Qiu was supported by the National Institutes of Health grant 1R01GM127922.

Author contributions

X. Liu produced and purified all proteins, and together with L. Rao performed the research; X. Liu, L. Rao, and A. Gennerich designed research; X. Liu, L. Rao, F. Berger, and A. Gennerich analyzed the experimental data; F. Berger derived the theoretical models for data fitting based on a WLC force-extension model; X. Liu, L. Rao, F. Berger, and A. Gennerich wrote the manuscript. A. Gennerich and W. Qiu secured funding.

Competing interests

The authors declare no competing interests.

Additional information

Supplementary information The online version contains supplementary material available at https://doi.org/10.1038/s41467-024-50990-x.

Correspondence and requests for materials should be addressed to Florian Berger or Arne Gennerich.

Peer review information *Nature Communications* thanks Erik Schäffer, and the other, anonymous, reviewer(s) for their contribution to the peer review of this work. A peer review file is available.

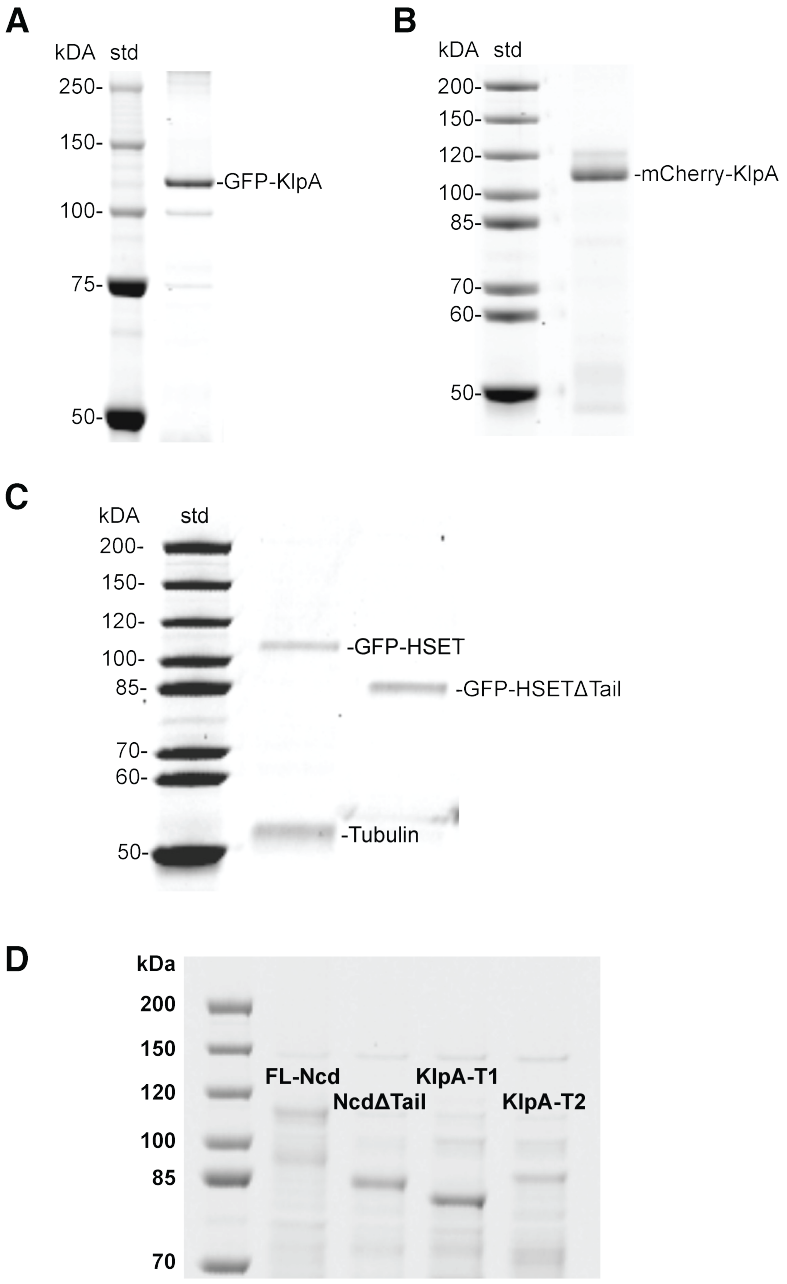

Suppl. Fig. 1 Sodium dodecyl-sulfate polyacrylamide gel electrophoresis (SDS-PAGE) gels. Molecular weight standards are indicated on each gel. (A) *E. Coli*-expressed GFP-KlpA. (B) *E. Coli*-expressed mCherry-KlpA. (C) Insect cell-expressed and MT-binding and -release purified GFP-HSET (left), and GFP-HSET-ΔTail (right). (D) *E. Coli*-expressed GFP-Ncd, GFP-Ncd-ΔTail, GFP-KlpA-T1, and GFP-KlpA-T2.

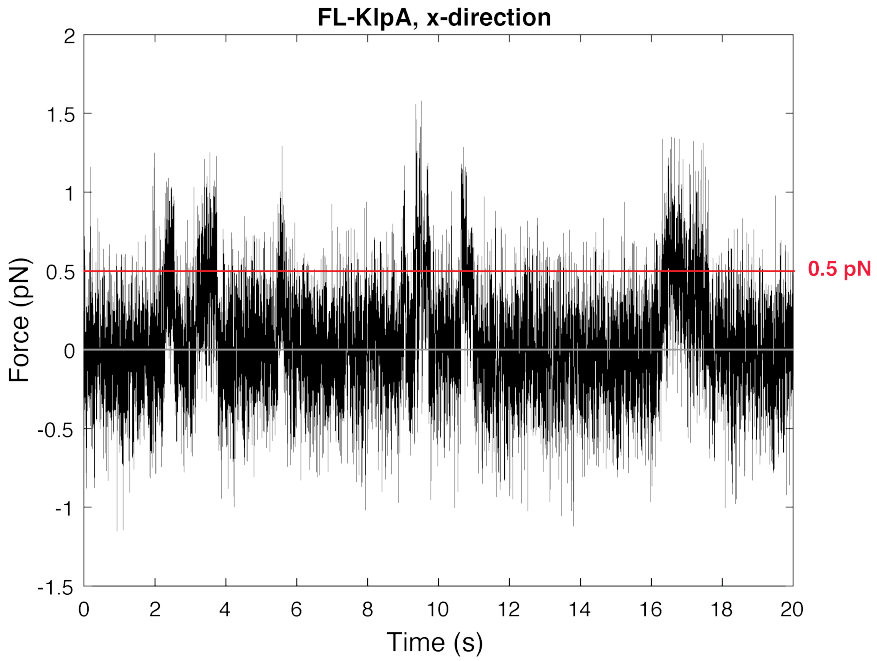

Suppl. Fig. 2 Force generation of a single full-length KlpA molecule. Representative force-versus-time trace showing bead movement driven by a single KlpA molecule at 1 mM ATP and k_{trap}=0.1 pN/nm in the *x*-direction (parallel to the long microtubule axis).

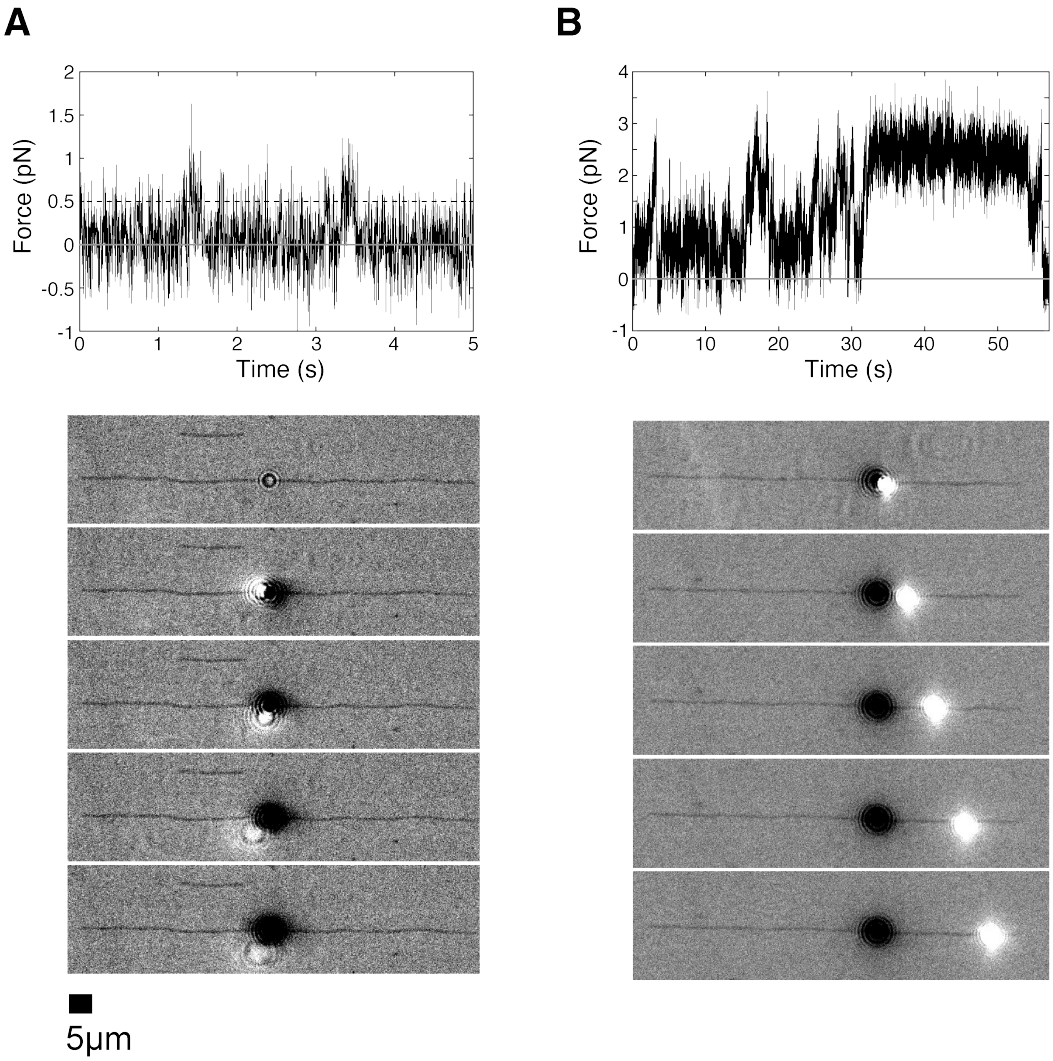

Suppl. Fig. 3 Interference reflection microscopy (IRM) images of the dynamic movement of beads coupled to KlpA molecules. (A) Top: Representative force-versus-time trace depicting bead movement driven by a single KlpA molecule at 1 mM ATP and k_{trap}=0.1 pN/nm. Bottom: Sequence of IRM images taken post-power stroke and following the deactivation of the optical trap, showing that a bead bound to a single KlpA molecule diffuses away from the MT following a single power stroke. (B) Top: As in *A*, but for a bead bound to multiple KlpA molecules at 1 mM ATP and k_{trap}=0.1 pN/nm. Bottom: Sequence of IRM images taken after the active multi-motor force generation and subsequent deactivation of the trapping laser, demonstrating that a bead bound to multiple KlpA molecules moves processively along the MT.

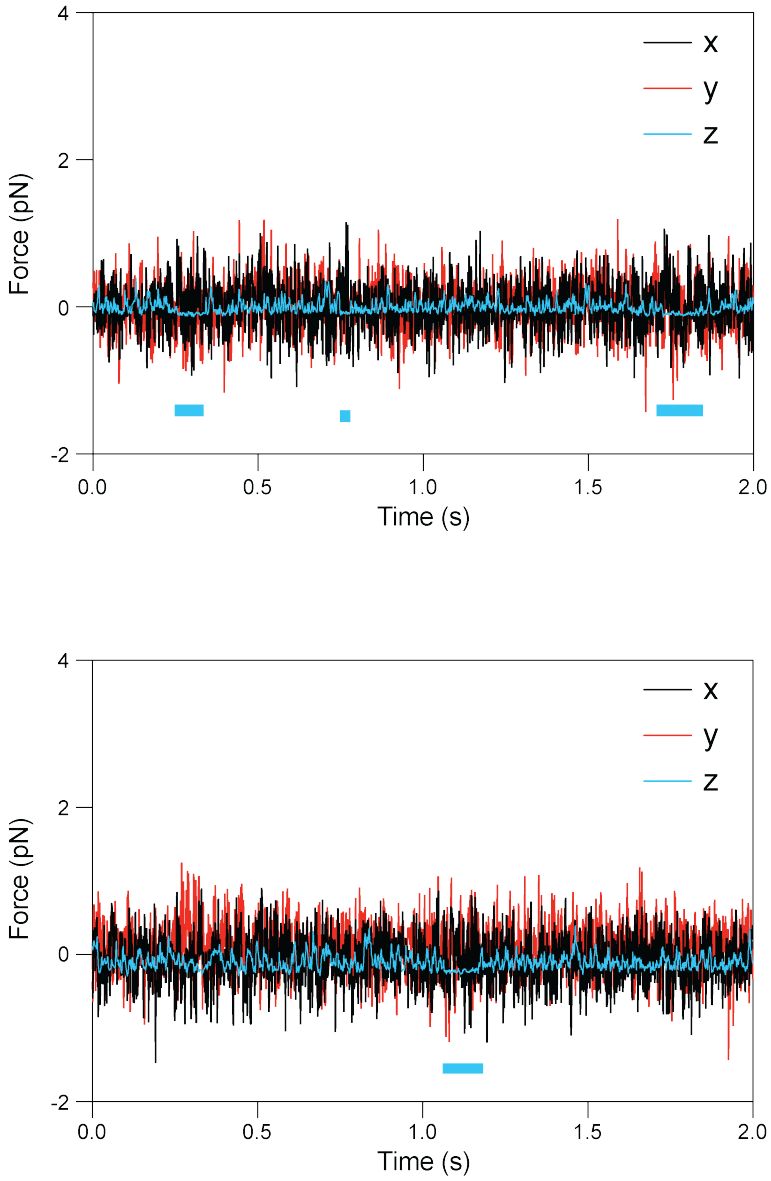

Suppl. Fig. 4 Interaction of a single full-length KlpA molecule with a MT in the absence of ATP/ADP. This figure shows optical trapping records demonstrating binding events between a single full-length KlpA molecule, attached to a 1-µm optical trapping bead, and a surface-attached MT. These interactions occur under conditions depleted of ATP and ADP by apyrase, leading to no measurable displacements in the *x* or *y* directions. Notably, the *z* signal's noise significantly decreases upon the motor's binding to the MT, as highlighted by the blue boxes. For enhanced visualization, the depicted traces were down-sampled by averaging 100 data points.

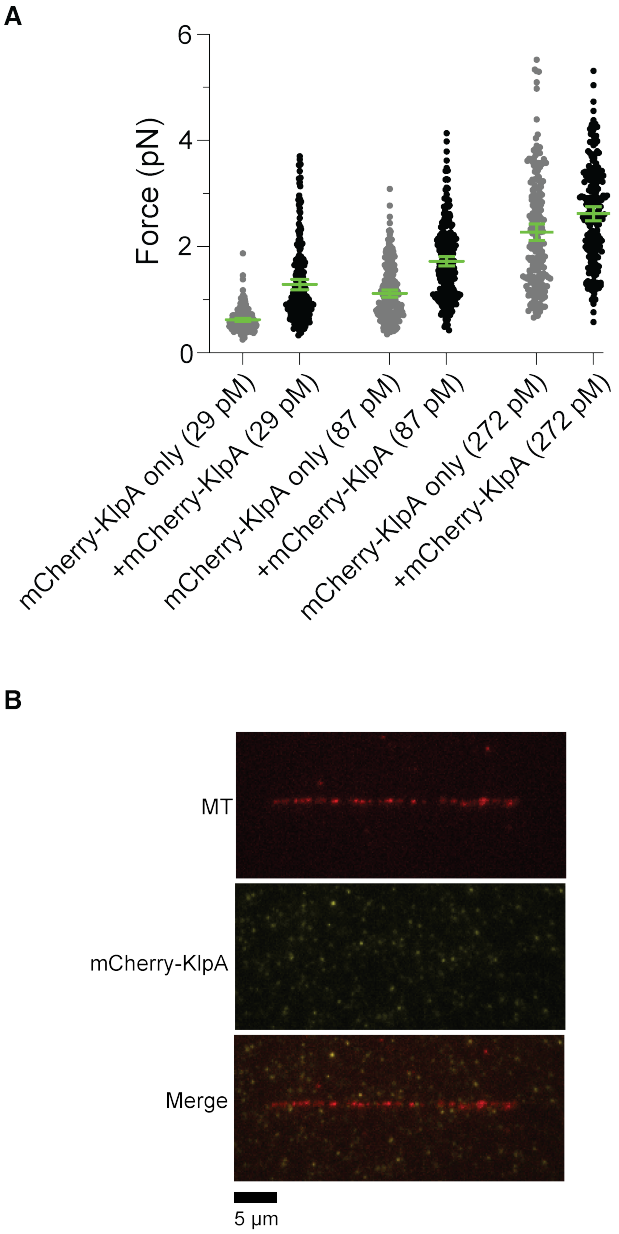

Suppl. Fig. 5 KlpA force generation as a function of increasing concentrations of mCherry-KlpA in the absence and presence of pre-bound GFP-KlpA. (A) Control experiments comparing the force differences of anti-GFP antibody-coated beads without (grey dots) and with pre-bound GFP-KlpA (black dots) in the presence of increasing concentrations of mCherry-KlpA at k_{trap}=0.05 pN/nm. Green bars represent the mean values with 95% CIs. 29 pM mCherry-KlpA

alone: 0.62 ± 0.01 pN pN (*n*=232); GFP-KlpA at the single-molecule level (14 pM) prebound to beads with added 29 pM mCherry-KlpA: 1.29 ± 0.05 pN (*n*=232); 87 pM mCherry-KlpA alone: 1.12 ± 0.03 pN (*n*=244); 14 pM GFP-KlpA plus 87 pM mCherry-KlpA: 1.73 ± 0.05 pN (*n*=259); 272 pM mCherry-KlpA alone: 2.27 ± 0.08 pN (*n*=188); 14 pM GFP-KlpA plus 272 pM mCherry-KlpA: 2.62 ± 0.07 pN (*n*=203). (B) TIRF image of GFP-KlpA at the single-molecule level (14 pM) prebound to beads with added 272 pM mCherry-KlpA.

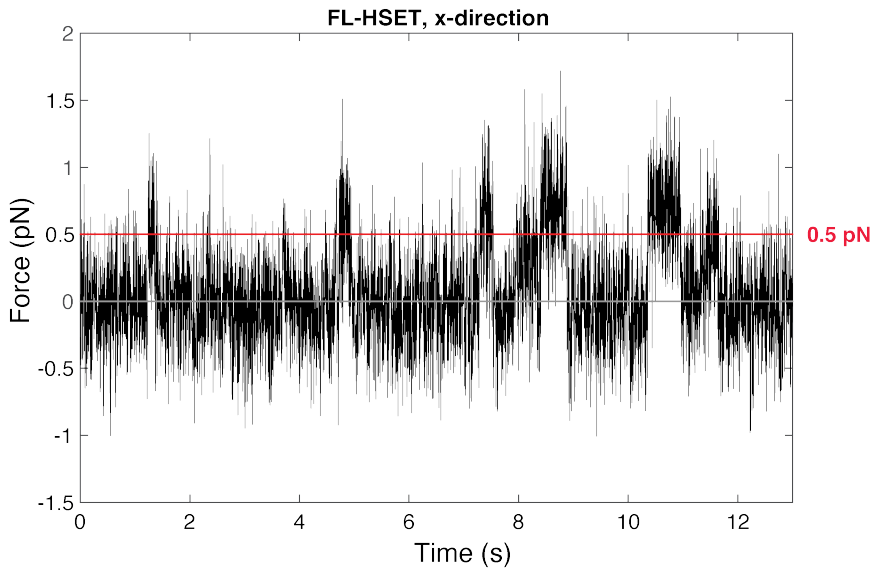

Suppl. Fig. 6 Force generation of a single full-length HSET molecule. Representative force-versus-time trace showing bead movement driven by a single HSET molecule at 1 mM ATP and k_{trap}=0.1 pN/nm in the *x*-direction (parallel to the long microtubule axis).

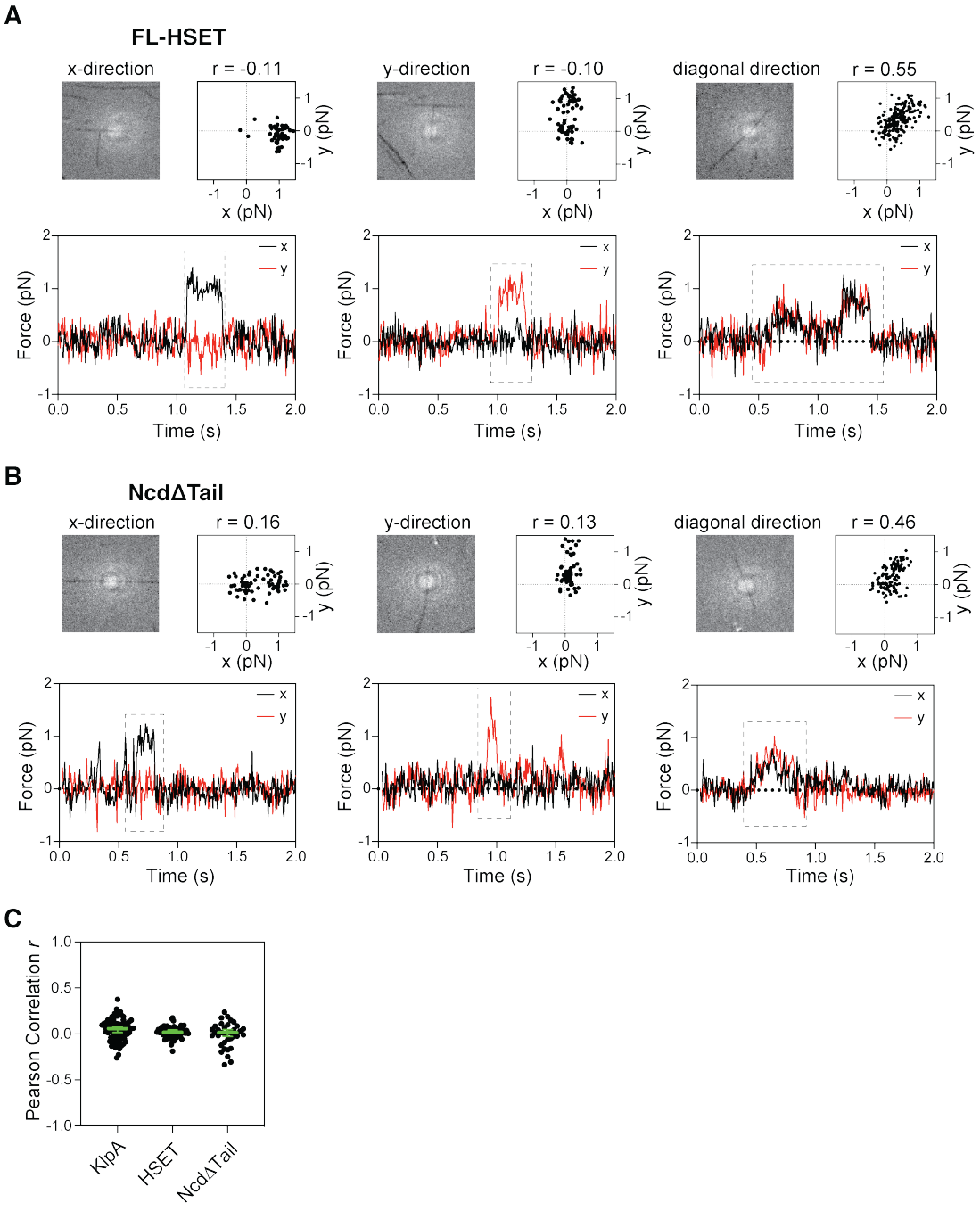

Suppl. Fig. 7 Kinesin-14 motors generate unidirectional displacements towards the MT minus end. (A) Full-length HSET exhibits power strokes towards the MT minus end, with no detectable displacements in the normal direction (Pearson correlation coefficient, $-0.2 < r < 0.2$). Top row: IRM images of horizontally and vertically oriented MTs and x-y position plots with Pearson correlation values. Bottom row: *x* (black) and *y* (red) direction signals. Diagonal MT

orientation shows displacements in both directions (right) (k_{trap}=0.1 pN/nm). (B) Similar to *A*, but for NcdΔTail. (C) The Pearson coefficients of correlation between *x*- and *y*-forces of power strokes for KlpA, HSET, and NcdΔTail on *x*-oriented MTs (k_{trap}=0.1 pN/nm). The green bars represent median values with 95% confidence interval. KlpA: 0.06 [0.01, 0.08], *n*=79; HSET: 0.02 [0.01, 0.04], *n*=61; NcdΔTail: 0.01 [-0.03, 0.04], *n*=36.

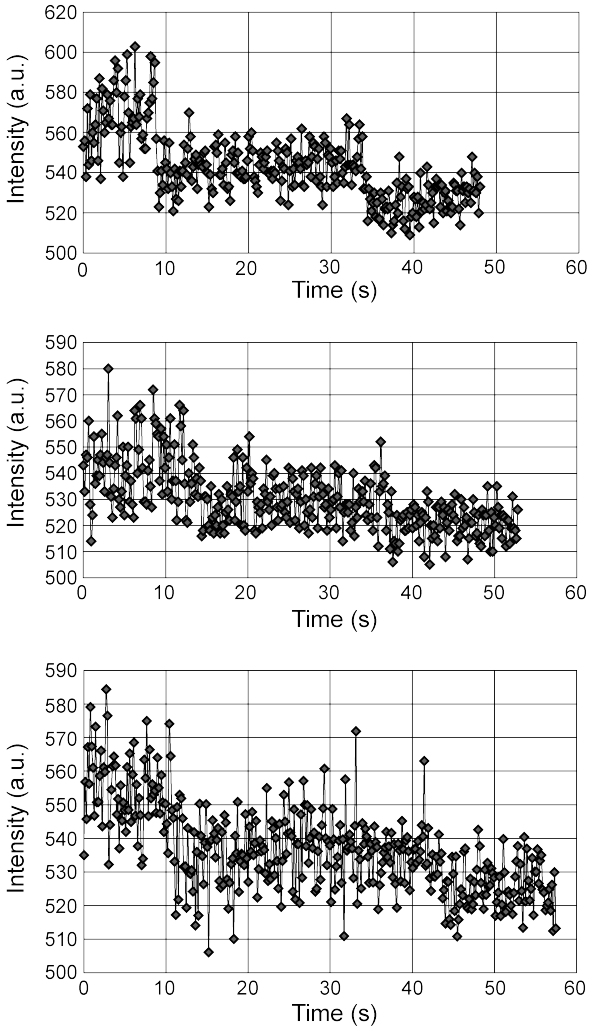

Suppl. Fig. 8 Fluorescence traces showing step-wise photobleaching of GFP-tagged HSET. Representative photobleaching examples showing GFP-HSET moelcules bleaching in two steps.

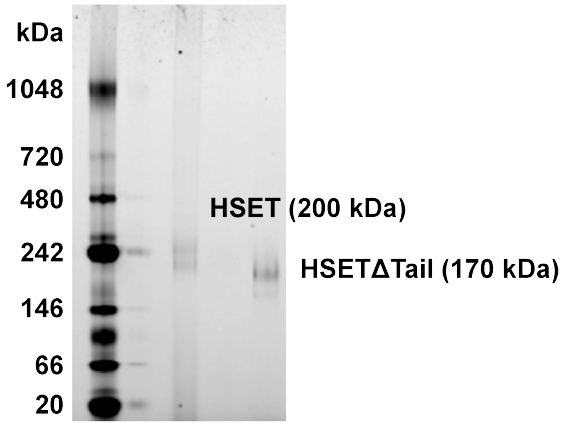

Suppl. Fig. 9 Native PAGE gel of HSET. A native PAGE gel of molecular mass marker (left), insect cell-expressed and MT-binding and -release purified GFP-HSET (middle), and GFP-HSET-ΔTail (right).

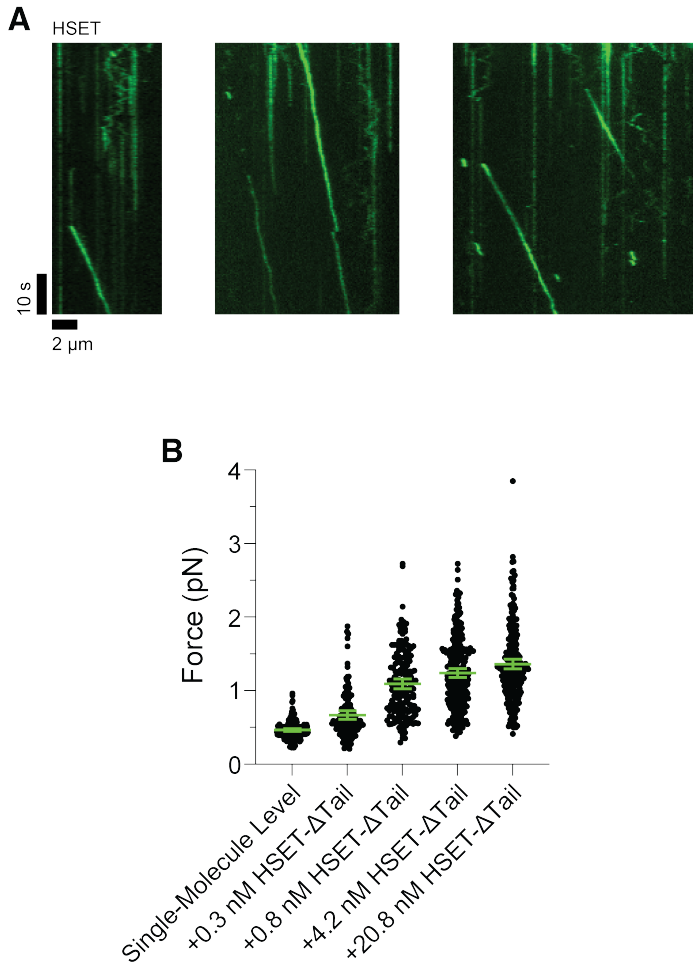

Suppl. Fig. 10 Processive motion of oligomerized HSET and force generation of GFP-HSET-ΔTail at increasing motor concentrations. (A) Examples of MT minus-end-directed processive motion of HSET particles formed at 1 nM motor concentration. These particles consist of multiple HSET motors working together. (B) Forces generated by GFP-HSET-ΔTail with increasing motor concentrations at k_{trap}=0.1 pN/nm. Green bars represent the mean values with 95% CIs. GFP-HSET-ΔTail at single-molecule level (30 pM): 0.46 ± 0.01 pN (*n*=197); +0.33 nM GFP-HSET-ΔTail: 0.67 ± 0.03 pN (*n*=124); +0.83 nM GFP-HSET-ΔTail: 1.09 ± 0.03 pN (*n*=170); +4.15 nM GFP-HSET-ΔTail: 1.24 ± 0.03 pN (*n*=252); +20.8 mM GFP-HSET-ΔTail: 1.36 ± 0.03 pN (*n*=236).

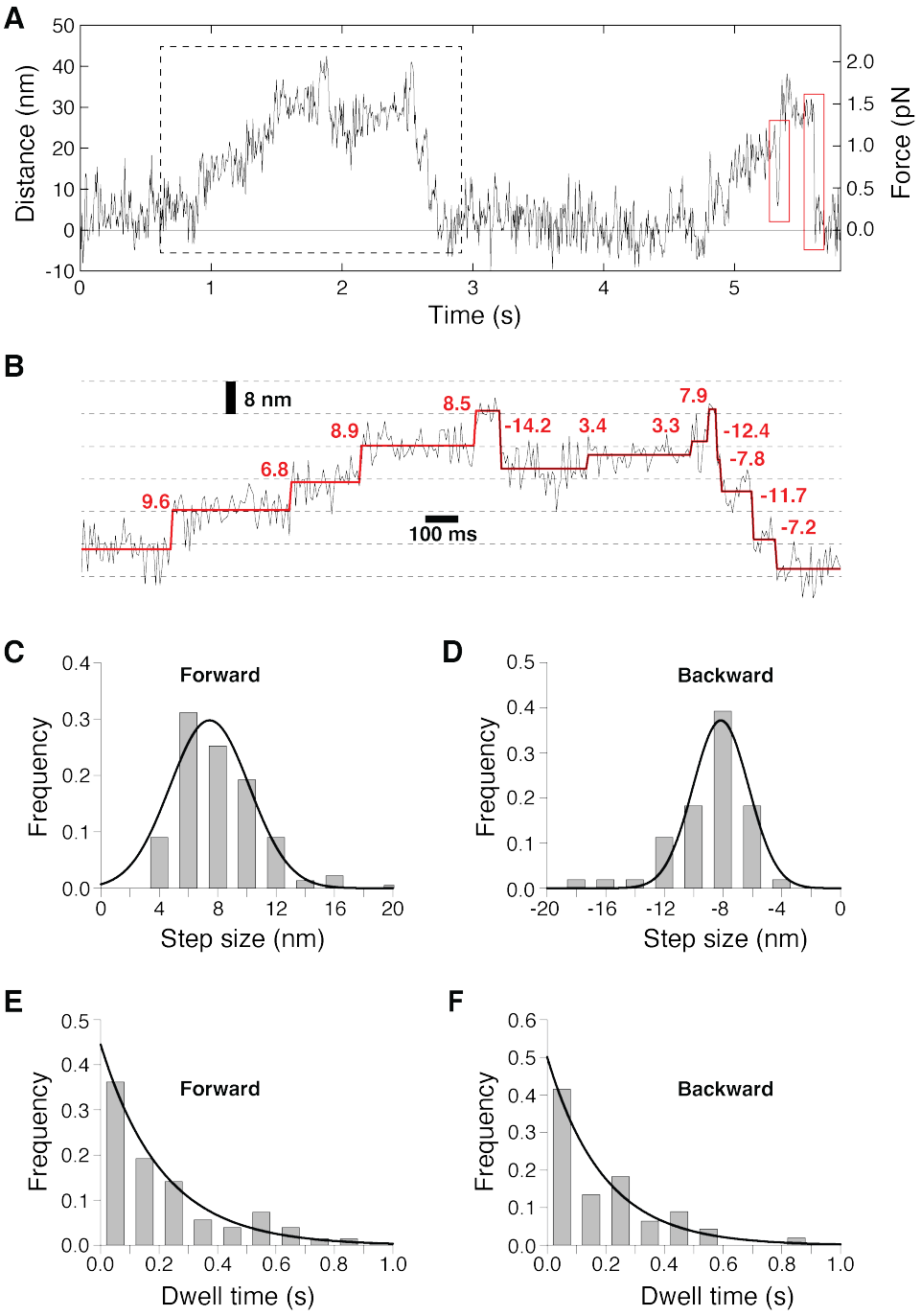

Suppl. Fig. 11 Stepping and dwell-time analysis of bead movement powered by multiple HSET molecules working together under loads of up to 1.5 pN. (A) Representative distance (force)-versus-time trace segment showing two subsequent force generation events. Motor slippage events, marked by the red boxes in the trace, were excluded from the analysis. (B) Fitting

of the data segment indicated by the dashed box in (A). The raw data are shown in black, and the steps detected by the step-finding program in red. (C) Histogram of detected forward steps (7.5 ± 0.3 nm, mean ± SEM from Gaussian fit, n=118). (D) As in *C*, but for the detected backward steps (-8.2 ± 0.2 nm, n=43). (E) Histogram of measured dwell times in-between steps (forward rate constant, k_f = 4.7 ± 0.43 s^{-1}, mean ± SEM from exponential fit). (F) As in *E*, but for measured dwell times after a backward step (backward rate constant, k_b = 5.2 ± 0.93 s^{-1}).

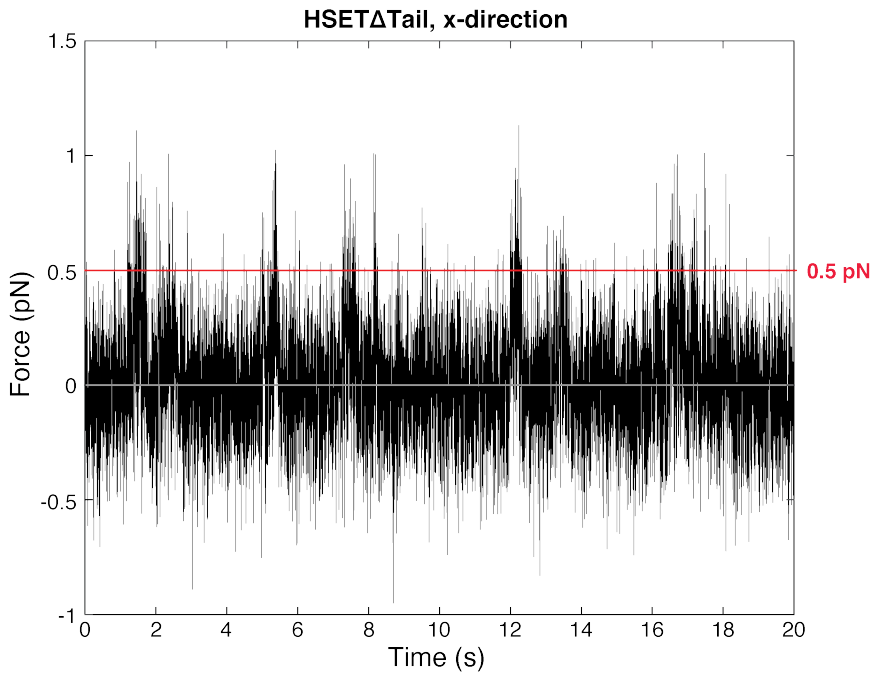

Suppl. Fig. 12 Force generation of a single HSETΔTail molecule. Representative force-versus-time trace showing bead movement driven by a single HSETΔTail molecule at 1 mM ATP and k_{trap}=0.1 pN/nm in the *x*-direction (parallel to the long microtubule axis).

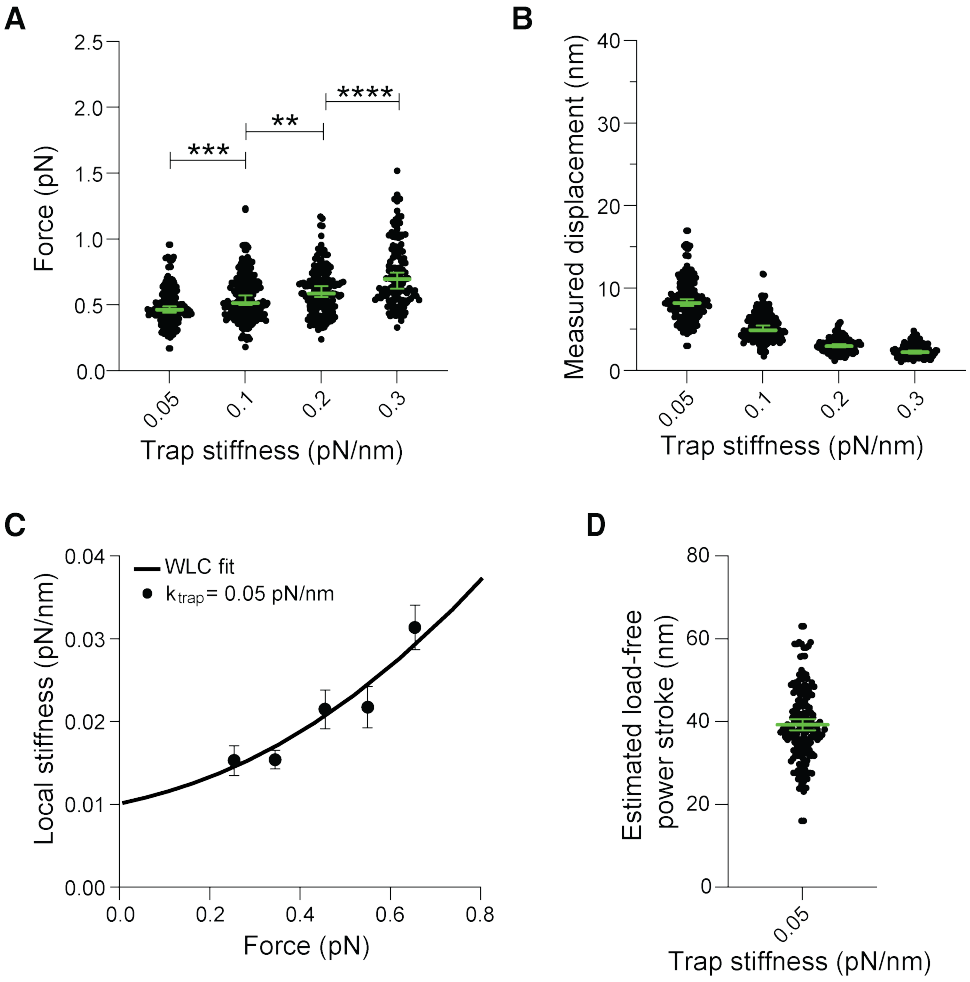

Suppl. Fig. 13 HSET power stroke and force generation as a function of trap stiffness. (A) Force generated by single HEST molecules as a function of increasing trap stiffnesses. Green bars indicate the median values with 95% CIs. k_{trap}=0.05 pN/nm: 0.46 (0.44, 0.49) pN (n=180); k_{trap}=0.1 pN/nm: 0.51 (0.50, 0.57) pN (n=214); k_{trap}=0.2 pN/nm: 0.59 (0.56, 0.64) pN (n=150); and k_{trap}=0.3 pN/nm: 0.69 (0.62, 0.74) pN (n=120). Statistical significance was determined using an unpaired Welch's t-test (**, P < 0.0066; ***, P < 0.0002; ****, P < 0.0001). (B) As in *A*, but for the measured displacements as a function of increasing trap stiffnesses. k_{trap}=0.05 pN/nm: 8.2 (7.8, 8.6) nm (n=180). k_{trap}=0.1 pN/nm: 4.9 (4.7, 5.4) nm (n=214); k_{trap}=0.2 pN/nm: 2.9 (2.8, 3.2) nm (n=150); and k_{trap}=0.3 pN/nm: 2.2 (2.0, 2.4) pN (n=120). (C) Measured local stiffness of full-length

HSET and bead linkage, $k_{\text{m-link}}$ (mean ± SEM), as function of force at 0.05 pN/nm trap stiffness (see Methods section for details underlying the stiffness calculations). The solid black line shows the fitted model, which considers the motor and bead-linkage as a worm-like chain (WLC) (see Methods for a description of the model and parameters used for fitting). (D) Estimated load-free power stroke at 0.05 pN/nm (see Methods section for a description of the calculation of the estimated load-free power strokes). Green bars indicate the mean value with 95% CIs: 39.4 (33.1, 45.1) nm (n=180).

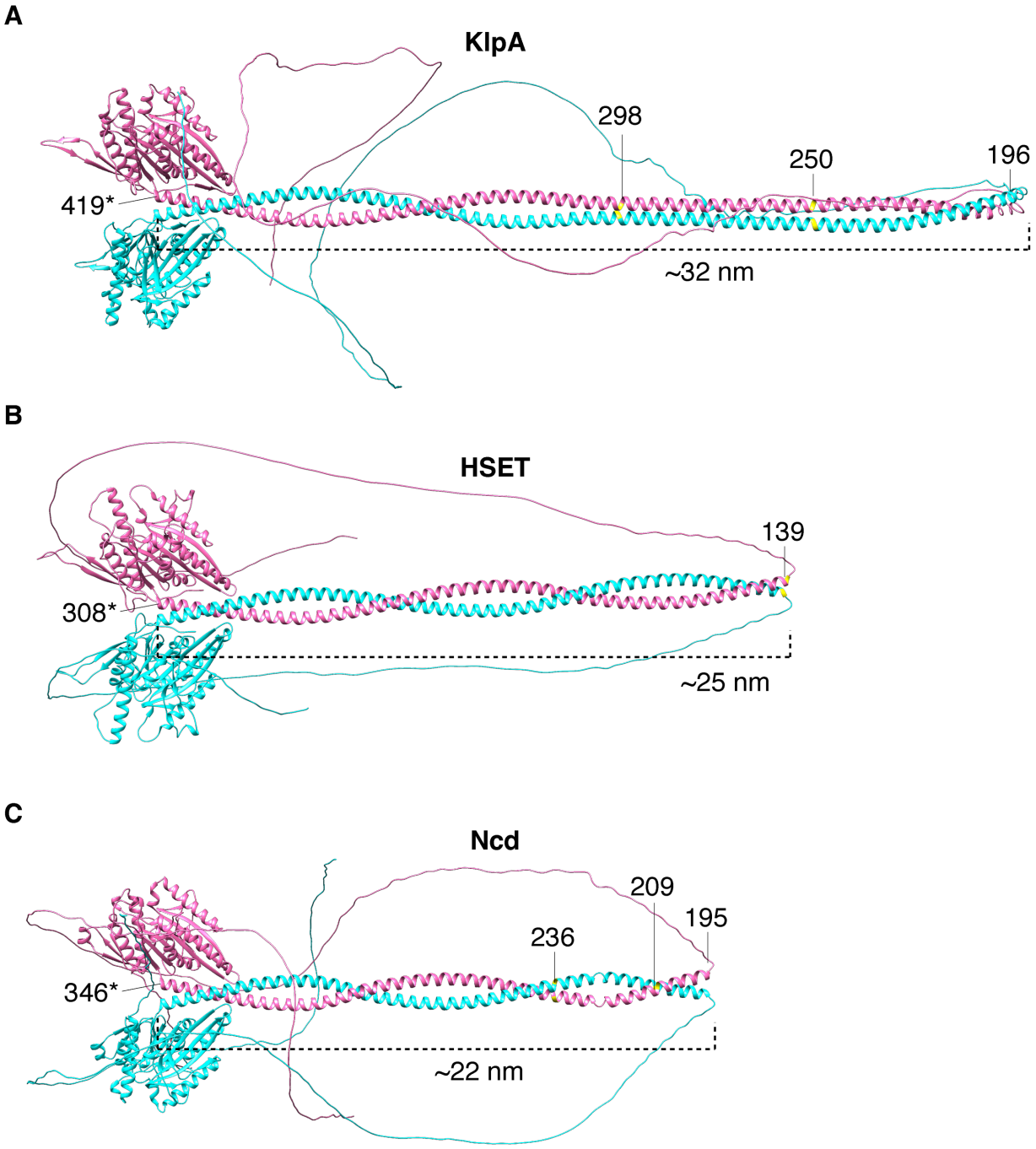

Suppl. Fig. 14 Structure prediction of Kinesin-14 molecules using ColabFold. (A) Predicted structure of KlpA (amino acids 1-770). The yellow-marked residues highlight the truncation sites for KlpA-T1 (amino acids 298-770) and KlpA-T2 (amino acids 250-770). The length of the

dimerizing coiled coil (amino acids 196-419) measures approximately 32 nm. (B) Predicted structure of HSET (amino acids 1-673). The yellow-marked residue highlights the truncation site for HSETΔTail (amino acids 139-673). The length of the dimerizing coiled coil (amino acids 139-308) measures approximately 25 nm. (C) Predicted structure of Ncd (amino acids 1-700). The yellow-marked residue highlights the truncating site for NcdΔTail (amino acids 209-700). The length of the dimerizing coiled coil (amino acids 195-346) measures approximately 22 nm.

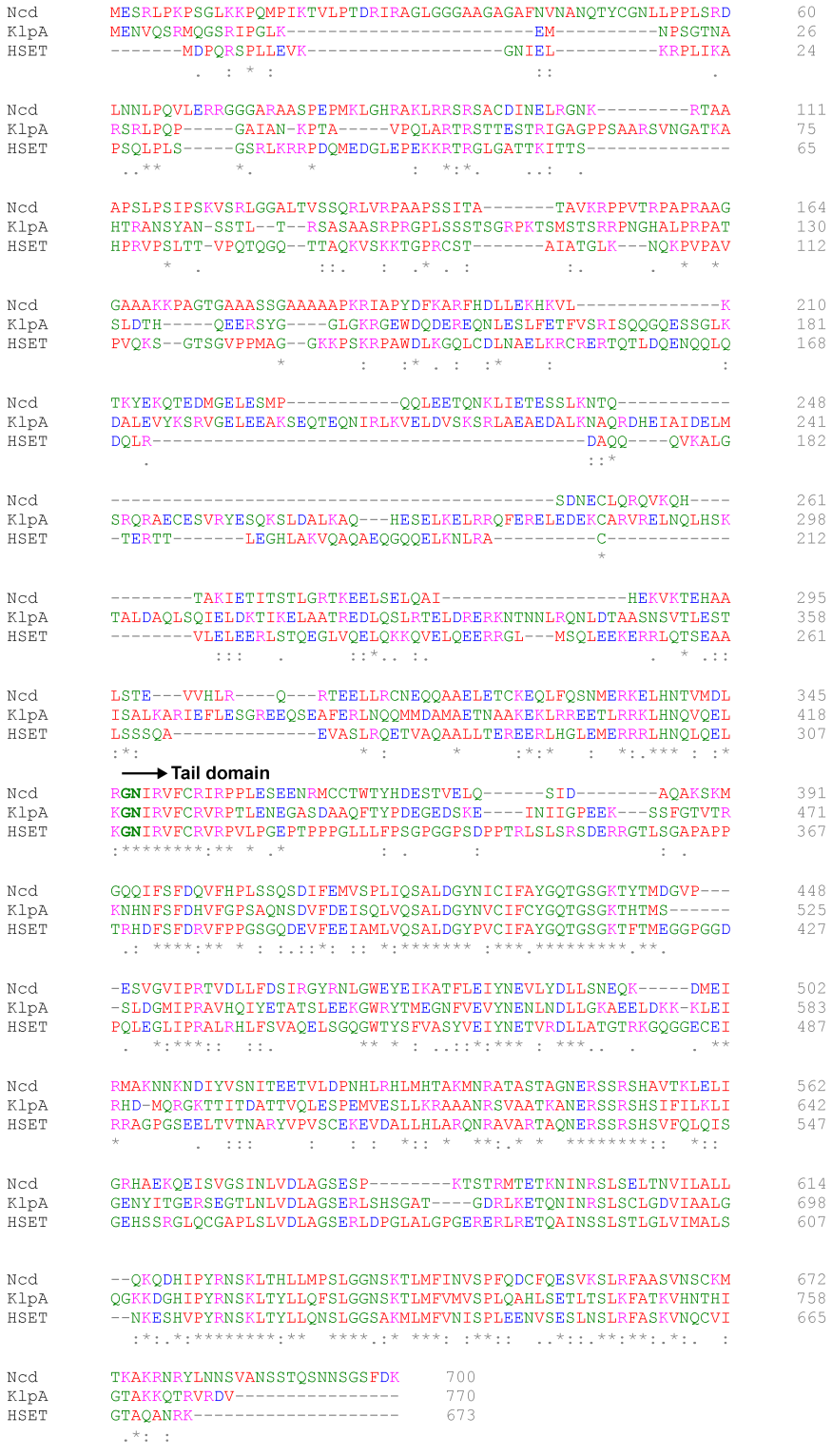

Suppl. Fig. 15 Sequence alignment of Ncd, KlpA and HSET. The black arrow indicates the beginning of the tail domain in each protein.

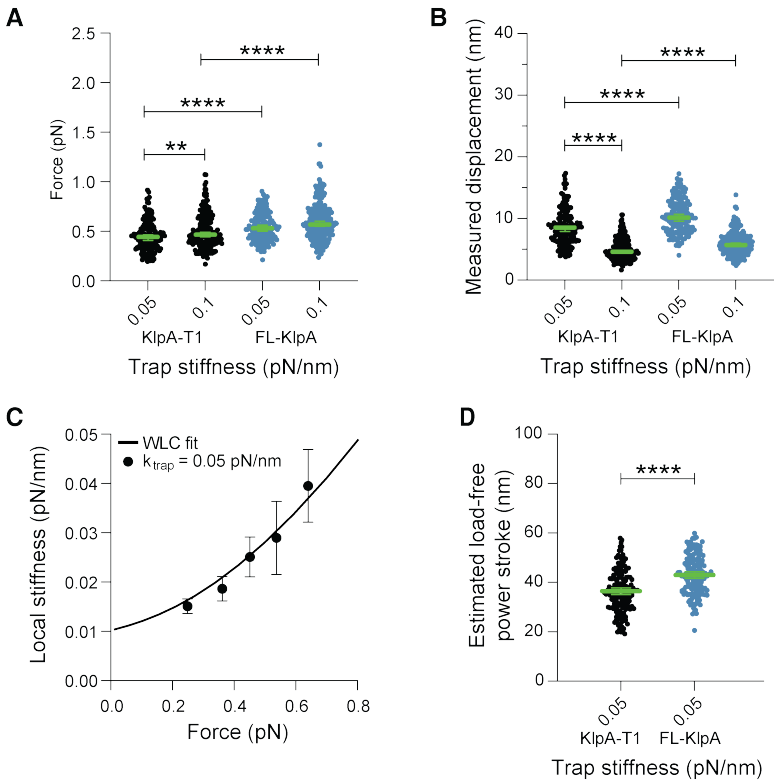

Suppl. Fig. 16 Force generation of single KlpA-T1 molecules as a function of trap stiffness and estimation of the load-free power stroke. (A) As in Fig. 3B, but for KlpA-T1 in comparison to full-length KlpA at the two lowest trap stiffnesses (full-length KlpA data reproduced from Fig. 3B). k_{trap}=0.05 pN/nm: 0.44 (0.41, 0.46) pN (n=152); k_{trap}=0.1 pN/nm: 0.46 (0.44, 0.49) pN (n=198); Statistical significance was determined using an unpaired Welch's t-test (**, P < 0.005; ****, P < 0.0001). (B) As in Fig. 3C, but for KlpA-T1 in comparison to full-length KlpA at the two lowest trap stiffnesses (full-length KlpA data reproduced from Fig. 3C). k_{trap}=0.05 pN/nm: 8.5 (7.9, 8.8) nm (n=152); and k_{trap}=0.1 pN/nm: 4.6 (4.4, 4.9) nm (n=198) (****, P < 0.0001) for KlpA-T1 (full-length KlpA data reproduced from Fig. 3C). (C) As in Fig. 3D, but for KlpA-T1 at the trap stiffnesses of 0.05 pN/nm. (D) As in Fig. 3E, but for KlpA-T1 in comparison to full-length KlpA at k_{trap}=0.05 pN/nm: 36.4 (30.0, 42.1) nm (n=152) for KlpA-T1 (full-length KlpA data reproduced from Fig. 3E) (****, P < 0.0001).

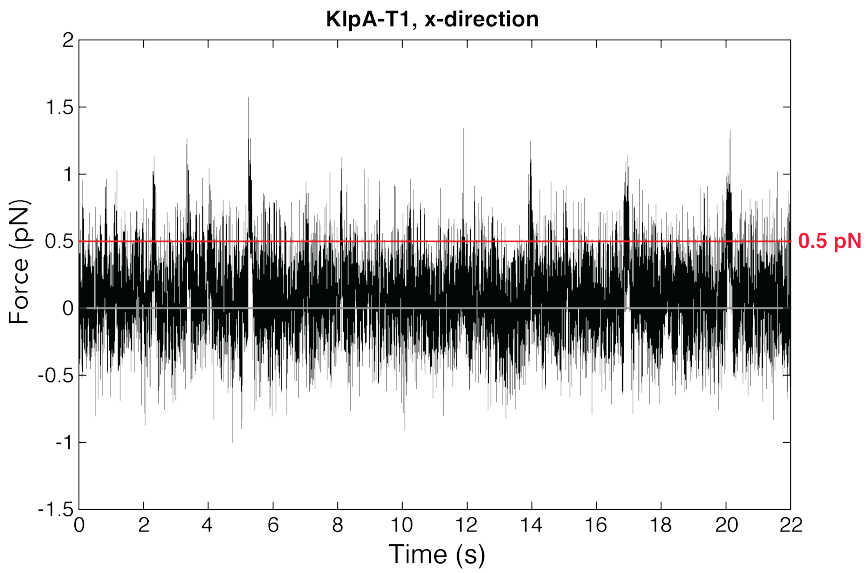

Suppl. Fig. 17 Force generation of a single KlpA-T1 molecule. Representative force-versus-time trace showing bead movement driven by a single KlpA molecule at 1 mM ATP and k_{trap}=0.1 pN/nm in the *x*-direction (parallel to the long MT axis).

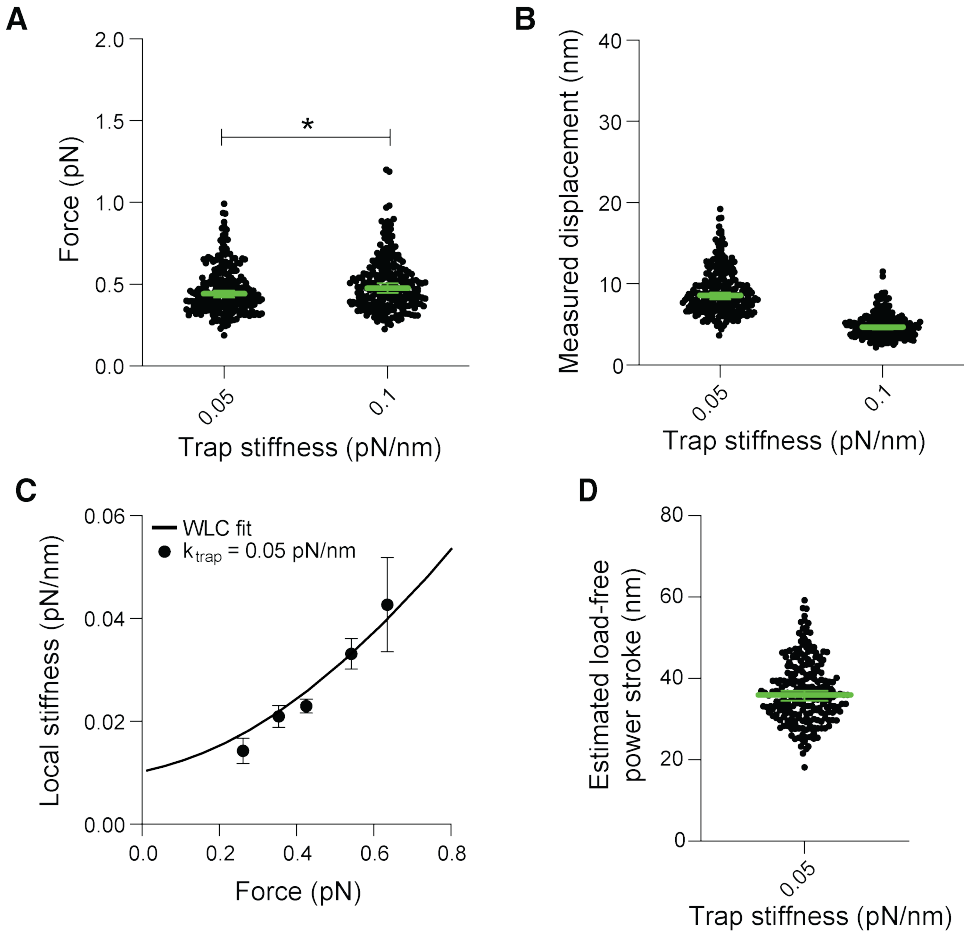

Suppl. Fig. 18 Force generation of single NcdΔTail molecules as a function of trap stiffness and estimation of the load-free power stroke. (A) As in Suppl. Fig. 3B, but for NcdΔTail at the two lowest trap stiffnesses. k_{trap}=0.05 pN/nm: 0.44 (0.42, 0.46) pN (n=236); and k_{trap}=0.1 pN/nm: 0.48 (0.45, 0.50) pN (n=227) (*, P < 0.028). (B) As in Fig. 3C, but for NcdΔTail at the two lowest trap stiffnesses. k_{trap}=0.05 pN/nm: 8.6 (8.1, 8.9) nm (n=236); and k_{trap}=0.1 pN/nm: 4.7 (4.4, 4.9) nm (n=227). (C) As in Fig. 3D, but for KlpA-T1 at the trap stiffnesses of 0.05 pN/nm. (D) As in Suppl. Fig. 3E, but for NcdΔTail at k_{trap}=0.05 pN/nm: 36.8 (31.4, 41.5) nm (n=236).

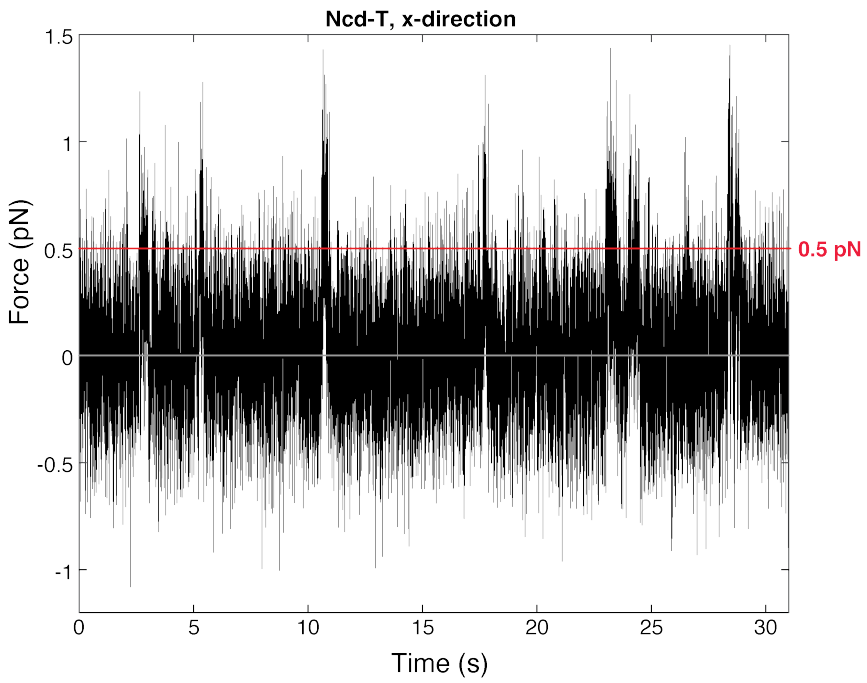

Suppl. Fig. 19 Force generation of a single NcdΔTail molecule. Representative force-versus-time trace showing bead movement driven by a single KlpA molecule at 1 mM ATP and k=0.1 pN/nm in the x-direction (parallel to the long MT axis).

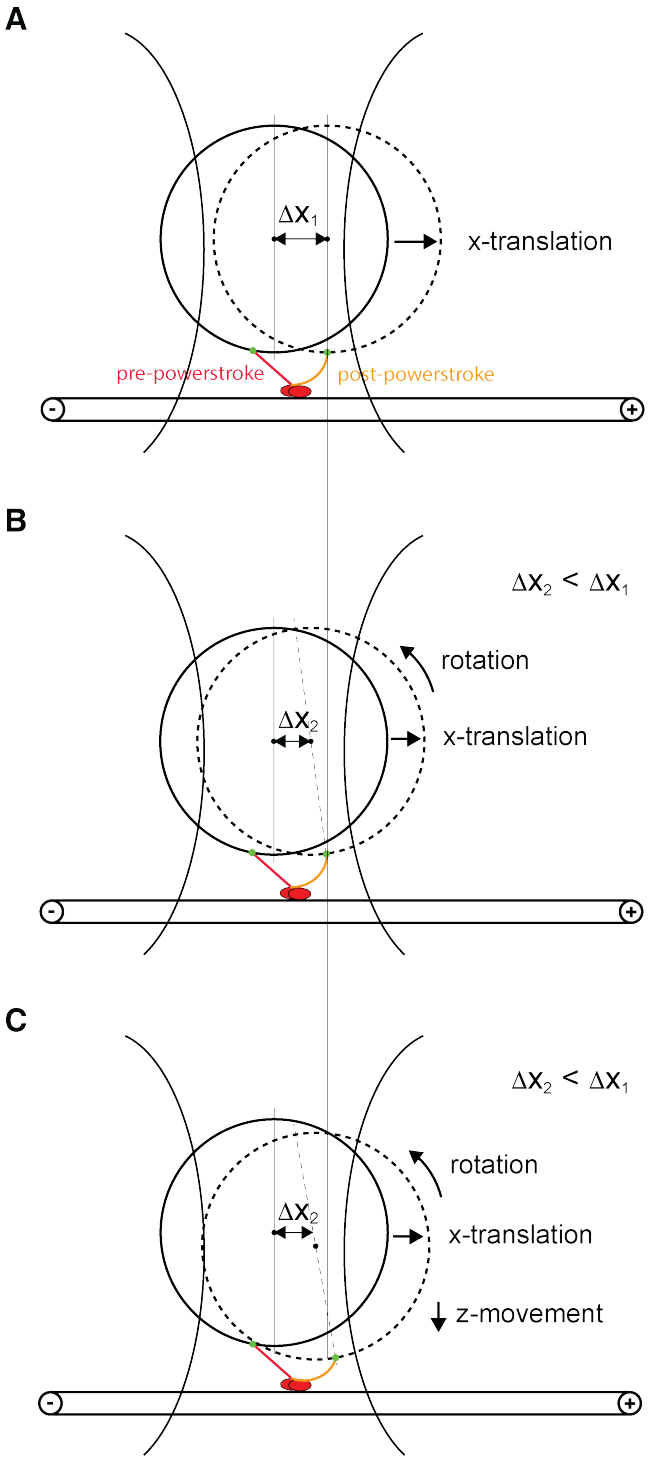

Suppl. Fig. 20 Illustrations of potential factors leading to an underestimation of the motor-generated power strokes. (A) The ideal scenario: Here, the motor's power stroke causes the attached bead to move solely along the *x*-axis. The displacement measured, ΔX_1, accurately

represents the true magnitude of the motor's power stroke, projected onto the *x*-axis, following compliance correction. (B) Realistic scenario: Here, the power stroke causes not just a translation of the bead but also its rotation. This dual effect leads to a measured displacement, ΔX_2, which is less than ΔX_1. (C) More complex scenario: When the bead is suited above the MT at a height that hinders interaction with the MT surface, the motor's power stroke results in translation, rotation, and a reduction in height (*z*). This multifaceted movement also results in a displacement ΔX_2 that is smaller than ΔX_1. Consequently, the measured and adjusted displacements reported in this work represent a minimum estimate of the motor's actual power-stroke magnitude. However, their closeness to the values predicted by AlphaFold suggests that the factors discussed have a limited impact.

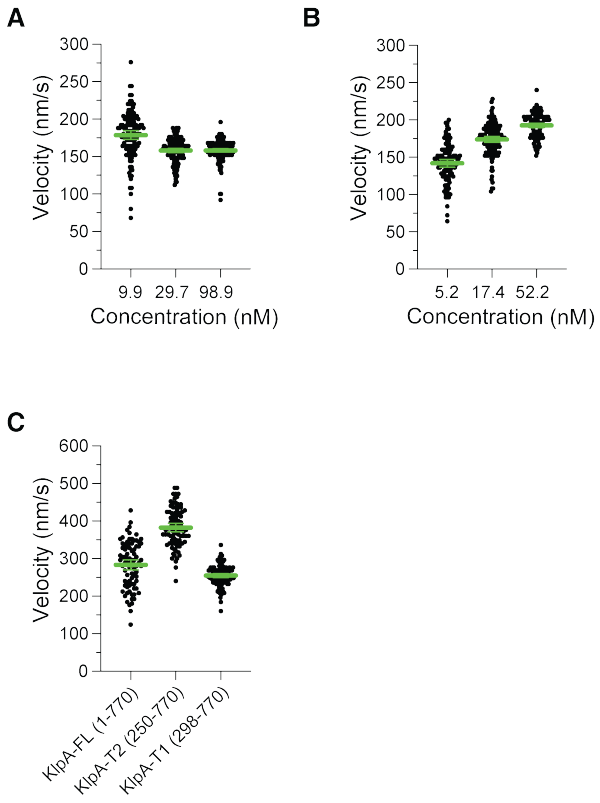

Suppl. Fig. 21 Cooperative effects of Kinesin-14 motor assemblies on MT-gliding velocity. (A) MT-gliding velocities as a function of increasing concentrations of full-length Ncd bound to the cover glass via anti-GFP antibodies. Green bars represent the mean values with 95% CIs. MT-gliding velocity at 9.9 nM: 178.7 ± 2.94 nm/s (*n*=122); 29.7 nM: 158.1 ± 1.42 nm/s (*n*=125); and 98.9 nM: 158.1 ± 1.2 nm/s (*n*=137). (B) MT-gliding velocities as a function of increasing concentrations of NcdΔTail bound to the cover glass via anti-GFP antibodies. Green bars represent the mean values with 95% CIs. MT-gliding velocity at 5.2 nM: 141.9 ± 2.67 nm/s (*n*=103); 17.4 nM: 173.8 ± 1.99 nm/s (*n*=126); and 52.2 nM: 192.7 ± 1.5 nm/s (*n*=115). (C) MT-gliding velocities of 9 nM KlpA, KlpA-T1 or KlpA-T2 bound to the cover glass via anti-GFP antibodies, respectively. Green bars represent the mean values with 95% CIs. MT-gliding velocity for KlpA: 283.3 ± 6.73 nm/s (*n*=83); for KlpA-T1: 254.6 ± 2.66 nm/s (*n*=107); and for KlpA-T2: 382.4 ± 5.59 nm/s (*n*=86).

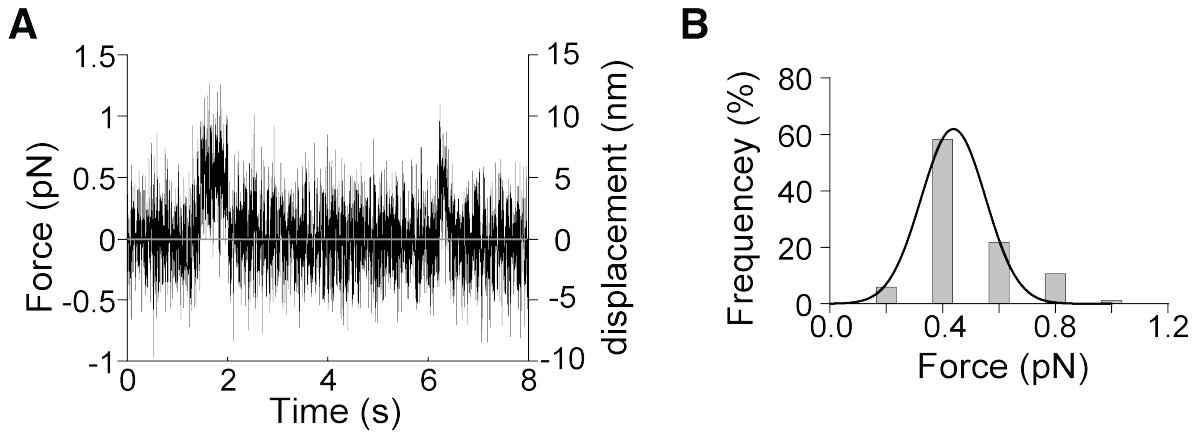

Suppl. Fig. 22 Force generation of a single *E. coli*-expressed GFP-HSET molecule. (A) Representative force-versus-time trace depicting bead movement driven by a single *E. coli*-expressed GFP-HSET molecule at 1 mM ATP and k_{trap}=0.1 pN/nm. (B) Histogram of forces generated by single GFP-HSET molecules (0.44 ± 0.014 pN, mean ± SEM from Gaussian fit, n=63).

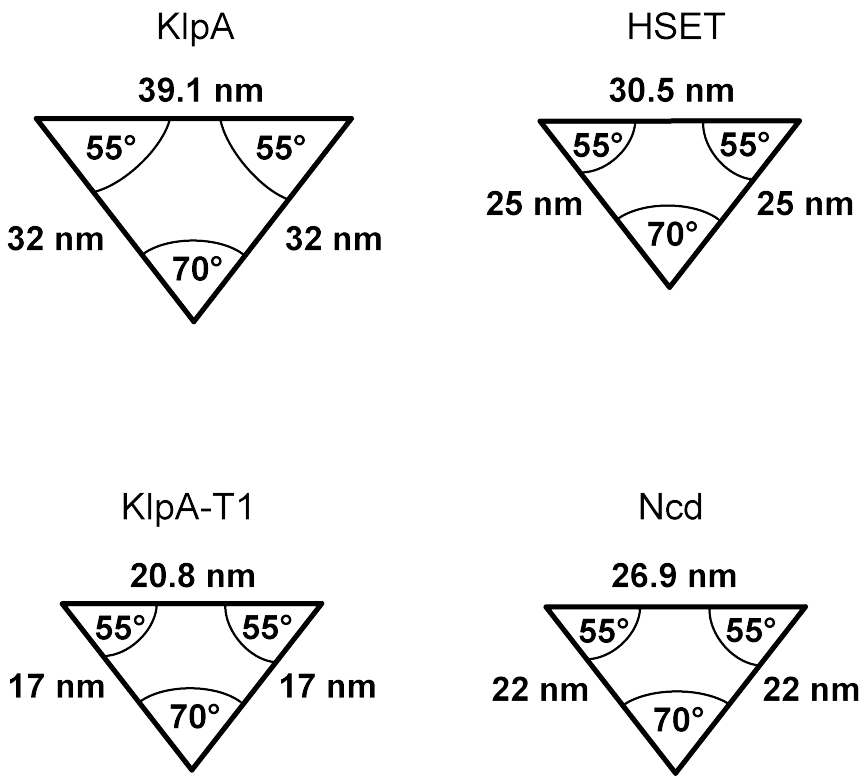

Suppl. Fig. 23 Power-stroke models for KlpA, HSET, KlpA-T1 and NcdΔTail. AlphaFold predicts coiled-coil lever arms of approximately 32 nm for full-length KlpA, 25 nm for full-length HSET, 17 nm for KlpA-T1, and 22 nm for NcdΔTail (refer to Suppl. Fig. 14). According to the cryoEM study on Ncd (Endres et al., Nature 2006), there is a 70° rotation of the lever arm toward the MT minus-end. Using these parameters, the estimated load-free power strokes are 39.1 nm for KlpA, 30.5 nm for HSET, 20.8 nm for KlpA-T1, and 26.9 nm for NcdΔTail.

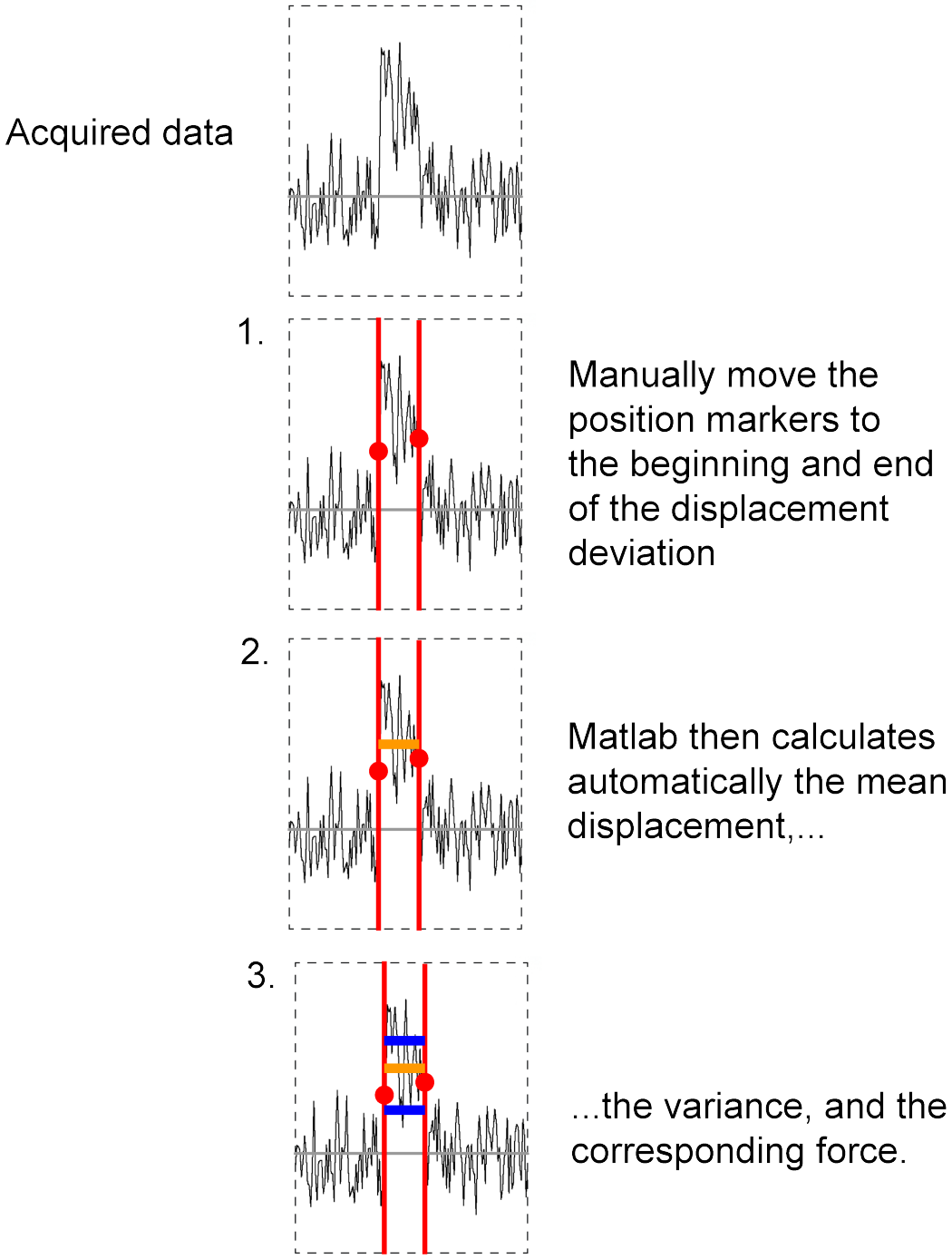

Suppl. Fig. 24 Schematic representation of the methodology for measuring a power stroke using a custom MATLAB program. See the Methods section "Analysis of optical trapping data" for more details.

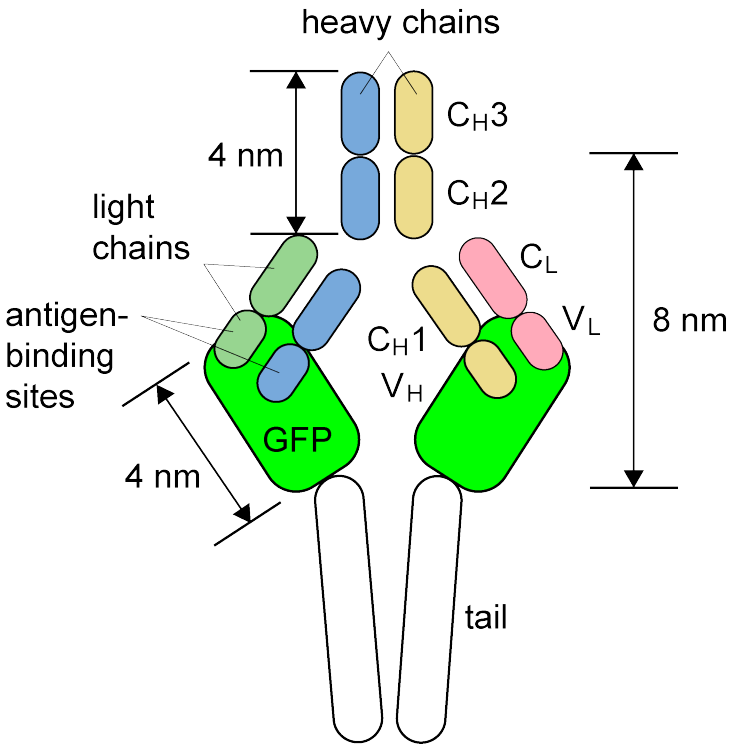

Suppl. Fig. 25 Illustration of the GFP-antibody complex size. Two GFP molecules are fused at their C-termini to the N-terminal tails of a dimeric Kinesin-14 motor and bind to the anti-GFP antibody. Since it is unknown which part of the antibody complex adheres to the bead surface during the cross-linking process, we estimate that approximately 8 nm effectively contributes to the length of the GFP-antibody bead linkage once the GFP is bound to the antigen-binding sites.